Influence of chiral symmetry on electron scattering at disordered graphene boundaries

Master thesis

by

Elias Walter

under the supervision of

Prof. Dr. Fabian Hassler
Institute for Quantum Information

2nd supervisor:

Prof. Dr. Christoph Stampfer
2nd Institute of Physics A

submitted to the

Faculty of Mathematics, Computer Science
and Natural Sciences
RWTH Aachen University

Aachen, 26. September 2017

Erklärung

Ich versichere hiermit an Eides Statt, dass ich die vorliegende Masterarbeit selbstständig und ohne unzulässige fremde Hilfe erbracht habe. Ich habe keine anderen als die angegebenen Quellen und Hilfsmittel benutzt.

Aachen, 26.09.2017

Elias Walter

Abstract

Since its discovery in 2004, graphene has drawn high interest from both experimental and theoretical side, and many possible applications, especially in nanoelectronics, have been proposed. Current graphene devices show extraordinarily high qualities, operating well in the ballistic regime. In graphene samples enabling ballistic transport in the bulk, scattering from the sample edges can become increasingly important. In this thesis, we study scattering processes at such disordered graphene boundaries. In particular, we investigate how the chiral symmetry of quasiparticles in graphene influences diffusive scattering. We find that a boundary that breaks chiral symmetry behaves like a mirror, in the sense that in the long Fermi wavelength limit diffusive scattering is suppressed and incoming electrons are reflected specularly. However, if the disorder on average preserves chiral symmetry, diffusive scattering increases significantly, leading to a breakdown of the mirror-like behavior.

Contents

1. Introduction

The carbon allotrope graphite has been used for hundreds of years and is still used extensively up to now for writing in pencils. The reason for this usability lies in its layered structure with strong covalent bonds within the layers but only weak van der Waals interactions that couple different layers, such that one can easily strip off stacks of graphite layers from a pencil onto a sheet of paper. [1]

Motivated by the possible use of graphite in nuclear reactors [1], in 1946 Wallace studied for the first time the electronic band structure of a single layer of graphite, called graphene, which consists of carbon atoms arranged in a so-called honeycomb lattice. He found an unusual linear dispersion close to the Fermi energy [2]. Semenoff showed in 1984 that due to this linear dispersion electrons in graphene behave like massless relativistic Dirac quasiparticles [3]. However, since it was long time thought that single layers of graphene were thermodynamically unstable [4], only in 2004 Novoselov and Geim and colleagues managed to isolate a single graphene layer by simple exfoliation, *i.e.*, removing excessive layers of a small piece of graphite by using a special tape [5]. By performing transport measurements on this single graphene sheet they could even proof the previously mentioned linear dispersion [6]. For these achievements they were awarded the 2010 Nobel prize in physics [7].

These discoveries gave rise to extensive studies of properties of graphene, both on experimental and theoretical side. Its unconventional electronic structure leads to a plethora of new phenomena and is therefore of big interest for fundamental research [4]. In 2005, Novoselov and Geim could for example experimentally show an anomaly in the integer quantum Hall effect in graphene [6]. Except for the relativistic nature of its quasiparticles, graphene has many more remarkable properties: As a one atom thin monolayer, it absorbs only $\sim 2.3\%$ of incident light and is therefore basically transparent. Due to the strong covalent bonds and its lattice structure, graphene is extremely robust against mechanical strength. Moreover, it has an extraordinarily high charge carrier mobility [7]. The aforementioned properties make graphene a promising candidate for various electronic applications [4]. As an example, the high mobility could make graphene-based transistors operating at clock rates of several hundred GHz possible, thus allowing for a speedup of two orders of magnitude compared to silicon-based transistors [8].

The basic components of such nanoelectronic graphene devices are graphene nanoribbons or nanoconstrictions. Recently, graphene devices with a mean free

path of more than $10\,\mu$m have been reported, which is of the order of typical sample sizes [9]. Therefore, electron transport in graphene nanoribbons can well reach the ballistic regime, where electrons barely scatter when passing through a sample. However, the sample edges will still show some roughness, and also the chemical passivation of the edges can lead to edge disorder. Thus, in devices where disorder in the bulk is weak, scattering on the sample edges becomes increasingly important and can be the main mechanism responsible for a decrease of the device conductance. For this reason it is of high interest for the development of graphene devices to understand the nature of scattering at such disordered boundaries.

In this thesis, we study the influence of disorder on electron scattering at a single graphene edge. The idealized system that we investigate corresponds to a graphene nanoribbon that we assume to be wide enough for the two edges to be considered as independent, such that one of the edges can safely be ignored. We compute scattering probabilities and phases at the remaining sample boundary within the formalism of the scattering matrix, to analyze how diffusive scattering depends on the strength of the disorder. Here we will keep a classical analogon in mind: Intuitively, we expect to see similarities to light scattering at a disordered surface. A clean smooth surface reflects light specularly, and the same is true for electrons scattering at a clean graphene boundary. Surface roughness or other types of disorder in both cases introduce diffusive scattering contributions. Based on these considerations, we also expect a graphene boundary to behave like a mirror. For weak enough disorder and long Fermi wavelengths, diffusive contributions should average out and scattering be largely dominated by specular reflection.

Additionally, Dirac fermions in graphene obey a so-called chiral symmetry due to the special lattice structure. This symmetry is typically broken by a boundary. However, tuning of the details of the disorder can also enable a preservation of this symmetry on average, even on a disordered boundary. As stated in the title, we will focus mainly on the influence of chiral symmetry on electron scattering. The most important insight of this thesis is that tuning the disorder such that chiral symmetry is preserved leads to a breakdown of the previously discussed mirror effect and hence to a significant increase of diffusive scattering.

The thesis is organized as follows. In Chapter 2 we will discuss basic properties of graphene that are relevant for the understanding of the work done in this thesis. After defining the graphene lattice in Section 2.1, we introduce two models our calculations are based on, the tight-binding approximation in Section 2.2 and the Dirac equation in Section 2.3. Both these approaches equivalently describe the low-energy physics of graphene. We also shortly comment on different types of graphene edges in Section 2.4. Chapter 3 is dedicated to the model that we will use to describe a disordered boundary and the techniques necessary to solve the scattering problem within this model. After introducing the general setup in

Sections 3.1 and 3.2, we will explain in Section 3.3 how to introduce a disordered boundary in the two approaches mentioned before. As chiral symmetry plays a major role for the scattering results, we discuss in Section 3.4 how it can be expressed within the model that we use. Next, in Section 3.5 we introduce the formalism of the scattering matrix used to compute scattering probabilities and phases. We conclude the chapter by further explaining the concept of self-averaging that was mentioned previously as mirror effect, in Section 3.6. In Chapter 4 we present an analytical derivation of the scattering matrix at the Dirac points, *i.e.*, at the Fermi energy of neutral graphene, and discuss the results depending on chiral symmetry, first from the Dirac equation in Section 4.1, and then extending the consideration to the tight-binding approximation in Section 4.2. Eventually, we generalize the discussion to any Fermi energy or doping of graphene by numerical studies in Chapter 5.

2. Graphene

2.1. Lattice structure

Graphene is a two-dimensional crystal allotrope of carbon. Carbon has the electron configuration $2s^2 2p^2$. In graphene, the $2s$ and $2p_x$ and $2p_y$ orbitals hybridize to form three sp^2 orbitals each filled by one electron, which are arranged in the xy-plane in a triangular shape with relative angles of 120°. These sp^2 hybrids form covalent bonds between neighboring carbon atoms, leading to the hexagonal structure depicted in Fig. 2.1, which is very robust against mechanical stress in the plane, but still very flexible due to its two-dimensionality. The sp^2 electrons form a deep lying σ band which is completely filled and does not contribute to electronic transport. The remaining p_z orbitals form a π band. Within graphite, the π electrons weakly couple single graphene layers, such that one can easily strip off layers when writing with a pencil. The π band is half-filled as it contains one electron per lattice site, and hence we will focus in this thesis on the electronic properties of the π electrons that are responsible for transport in graphene. [1]

Particularly noticeable is the fact that the hexagonal graphene lattice is no Bravais lattice, such that we describe it as a triangular lattice with a two-atomic basis. The fundamental lattice vectors are given by

$$\boldsymbol{a}_1 = \begin{pmatrix} a \\ 0 \end{pmatrix}, \quad \boldsymbol{a}_2 = \frac{a}{2} \begin{pmatrix} 1 \\ \sqrt{3} \end{pmatrix}, \tag{2.1.1}$$

with the lattice constant $a \approx 2.46\,\text{Å}$ (Fig. 2.1). The vectors between nearest neighbors belonging to different sublattices are given by

$$\boldsymbol{\delta}_1 = \begin{pmatrix} 0 \\ a_0 \end{pmatrix}, \quad \boldsymbol{\delta}_2 = \frac{a_0}{2} \begin{pmatrix} \sqrt{3} \\ -1 \end{pmatrix}, \quad \boldsymbol{\delta}_3 = \frac{a_0}{2} \begin{pmatrix} -\sqrt{3} \\ -1 \end{pmatrix}, \tag{2.1.2}$$

with the carbon-carbon distance $a_0 = a/\sqrt{3} \approx 1.42\,\text{Å}$. The reciprocal lattice is as well triangular with lattice vectors

$$\boldsymbol{b}_1 = \frac{2\pi}{a\sqrt{3}} \begin{pmatrix} \sqrt{3} \\ -1 \end{pmatrix}, \quad \boldsymbol{b}_2 = \frac{4\pi}{a\sqrt{3}} \begin{pmatrix} 0 \\ 1 \end{pmatrix}. \tag{2.1.3}$$

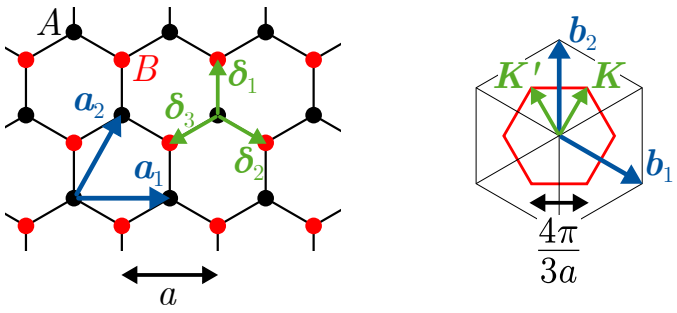

Figure 2.1.: Left: Graphene lattice, consisting of two Bravais sublattices A (black) and B (red). The lattice constant is given by $a \approx 2.46\,\text{Å}$. Lattice vectors are $\boldsymbol{a}_1$ and $\boldsymbol{a}_2$ and the vectors connecting nearest neighbors are called $\boldsymbol{\delta}_1$, $\boldsymbol{\delta}_2$, $\boldsymbol{\delta}_3$. Right: Reciprocal lattice of the triangular sublattice of graphene with lattice vectors $\boldsymbol{b}_1$ and $\boldsymbol{b}_2$. The first Brillouin zone is drawn in red. The corners of the first Brillouin zone $\boldsymbol{K}$ and $\boldsymbol{K'}$ are called Dirac points.

The so-called Dirac points at the corners of the first Brillouin zone have a particular importance for the electronic band structure as we will see later. There are six of them, of which however always three are equivalent up to shifting by a reciprocal lattice vector. Therefore, we have two distinct Dirac points denoted

$$\boldsymbol{K} = \frac{2\pi}{3a}\begin{pmatrix} 1 \\ \sqrt{3} \end{pmatrix} \quad \text{and} \quad \boldsymbol{K'} = \frac{2\pi}{3a}\begin{pmatrix} -1 \\ \sqrt{3} \end{pmatrix} . \tag{2.1.4}$$

2.2. Electronic properties in the tight-binding approximation

Since we consider a single electron in a $2p_z$ orbital per lattice site, it is convenient to start the description of electronic properties of graphene from a tight-binding model. Within this approach, we express the single-particle lattice Hamiltonian in the basis $\{|j\rangle\}$ of atomic orbitals living on distinct lattice sites labeled by j,

$$H = \sum_{i,j} H_{ij} |i\rangle\langle j| \,, \tag{2.2.1}$$

where $H_{ij} = \langle i|H|j\rangle$ is the amplitude of hopping from lattice site j to lattice i for $i \neq j$. The nearest-neighbor hopping is determined as $-t \approx -2.8\,\text{eV}$ and the next nearest-neighbor hopping can be estimated to be roughly $-t' \approx -0.1\,\text{eV}$. Note that this model is non-interacting. This is a reasonable approximation in the low-

energy regime of graphene, where electron-electron interactions are typically weak. Moreover, we ignore the electron spin, since spin-orbit interactions are negligible as well and we do not take any magnetic fields into account. [1]

Since $t' \ll t$, and higher order hoppings are even smaller, within the nearest-neighbor tight-binding approximation we assume that electrons are tightly bound to the lattice sites and can only hop to neighboring sites, such that all hoppings of higher order than t are zero. In this approximation the Hamiltonian becomes

$$H = -t \sum_{\langle i,j \rangle} |i\rangle\langle j| \,, \tag{2.2.2}$$

where the brackets indicate that the sum goes only over pairs of nearest neighbors. The onsite energies H_{ii} just fix from where we measure the chemical potential and can therefore be set to zero.

We can express the atomic orbital states $|j\rangle$ as the Fourier transform of Bloch states $|\boldsymbol{k}\rangle$. Since the graphene lattice consists of two distinct Bravais sublattices, we have to do this for A and B sites separately. For site j at position $\boldsymbol{r}_j^{(A)}$ belonging to sublattice A, we hence write

$$|j\rangle_A = \frac{1}{\sqrt{N}} \sum_{\boldsymbol{k}} e^{-i\boldsymbol{k}\cdot\boldsymbol{r}_j^{(A)}} |\boldsymbol{k}\rangle_A \,, \tag{2.2.3}$$

with the number of lattice sites N, and equivalently for sublattice B. By inserting this into Eq. (2.2.2), followed by simple geometrical considerations, we obtain

$$H = -t \sum_{\boldsymbol{k}} \Big(f(\boldsymbol{k}) |\boldsymbol{k}\rangle_A \langle \boldsymbol{k}|_B + \text{h.c.} \Big) \,, \tag{2.2.4}$$

with $f(\boldsymbol{k}) = \sum_{j=1}^{3} e^{i\boldsymbol{k}\cdot\boldsymbol{\delta}_j}$. We can write the Hamiltonian for each $\boldsymbol{k}$ in matrix form as

$$H(\boldsymbol{k}) = -t \begin{pmatrix} 0 & f(\boldsymbol{k}) \\ f^*(\boldsymbol{k}) & 0 \end{pmatrix} \,, \tag{2.2.5}$$

indicating that it acts on a spinor wavefunction $\psi = (\psi_A, \psi_B)^T$.

As the Hamiltonian of Eq. (2.2.4) is diagonal in momentum space, we can directly read of its band structure, which is given by

$$E_\pm(\boldsymbol{k}) = \pm t |f(\boldsymbol{k})| = \pm t \sqrt{2\cos(k_x a) + 4\cos\left(\frac{k_x a}{2}\right)\cos\left(\frac{k_y a\sqrt{3}}{2}\right) + 3} \,. \tag{2.2.6}$$

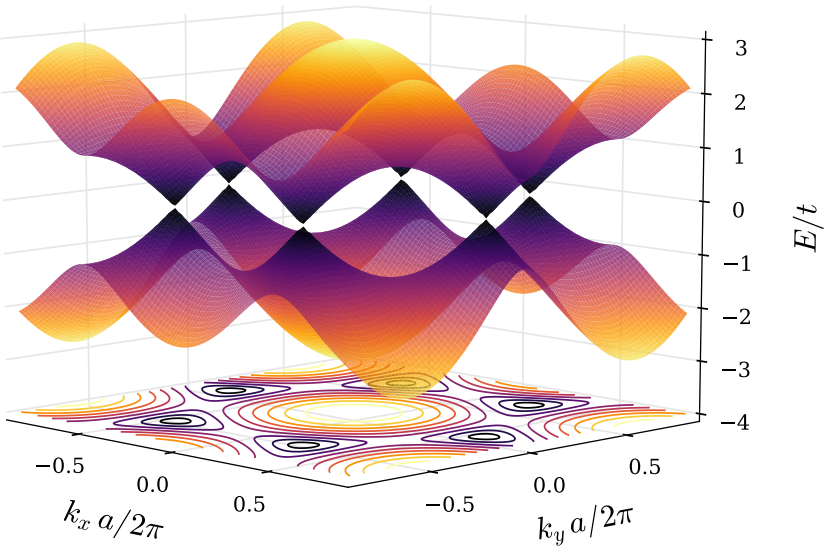

Figure 2.2.: Band structure of graphene within the first Brillouin zone (1BZ). At the Dirac points at the corners of the 1BZ the dispersion is linear and gapless. The projection shows the six-fold symmetry in momentum space around $\boldsymbol{k} = 0$.

This form was first obtained in [2]. The band structure is plotted in Fig. 2.2. We obtain a gapless dispersion that is symmetric around $E = 0$ and can be divided into two bands. Since each lattice site contributes one free electron, at zero temperature the Fermi energy lies at $E = 0$, such that the lower band is completely filled and the upper band is empty. Low-energy excitations are possible at the corners of the first Brillouin zone where the two bands touch. At these Dirac points the dispersion is linear, contrary to the usual quadratic shape of (approximately) free electrons. The cone-like dispersion indicates massless relativistic Dirac quasiparticles as discussed further on.

Expanding the dispersion around the Dirac points, with $\boldsymbol{k} = \boldsymbol{K} + \boldsymbol{q}$ we obtain

$$E_{\pm}(\boldsymbol{q}) = \pm\hbar v_F |\boldsymbol{q}| + \mathcal{O}(\boldsymbol{q}^2)\,, \tag{2.2.7}$$

as also discussed in [2], with the Fermi velocity

$$v_F = \frac{\sqrt{3}ta}{2\hbar} \approx 10^6 \,\mathrm{m/s}\ [1]\,, \tag{2.2.8}$$

which is—remarkably—a constant and does not depend on $\boldsymbol{k}$. In the low-energy regime the Fermi wavelength is accordingly given in terms of the Fermi energy E_F by

$$\lambda_F = \frac{2\pi}{k_F} = \frac{\sqrt{3}\pi ta}{E_F}\,. \tag{2.2.9}$$

2.3. Dirac approximation

Due to the linearity of the dispersion, the low-energy regime of electrons in graphene can as well be described by the massless Dirac equation. In doing so, we completely omit the lattice and go to a continuum model, which can be derived from the tight-binding model as follows. It is shown in [3] that expanding the tight-binding Hamiltonian of Eq. (2.2.5) around $\boldsymbol{K}$ and $\boldsymbol{K'}$, we obtain

$$H = v_F \tau_0 \otimes (\boldsymbol{\sigma} \cdot \boldsymbol{p})\,. \tag{2.3.1}$$

This Hamiltonian acts on the combined valley and sublattice space $\mathcal{H}_V \otimes \mathcal{H}_S$. By $(\tau_0, \tau_x, \tau_y, \tau_z)$ we denote the identity and Pauli matrices in the two-dimensional subspace $\mathcal{H}_V$ that is spanned by the two distinct Dirac cones (or valleys) $\boldsymbol{K}$ and $\boldsymbol{K'}$. We call $\boldsymbol{\sigma} = (\sigma_x, \sigma_y)^T$ the vector of Pauli matrices in the two-dimensional sublattice space $\mathcal{H}_S$, and $\boldsymbol{p} = \hbar\boldsymbol{q}$. We expressed H in the valley-isotropic representation that is also used in [10].

With this 4×4 Hamiltonian the Schrödinger equation $H\psi = E\psi$ becomes the Dirac equation for massless relativistic particles, which is therefore the nature of excitations in graphene. These quasiparticles are described by 4-spinor wavefunctions living on $\mathcal{H}_V \otimes \mathcal{H}_S$. The sublattice degree of freedom can be interpreted as a pseudospin, expressed by $\boldsymbol{\sigma}$, which Dirac fermions in graphene possess. The spin directions $\uparrow$ and $\downarrow$ of this pseudospin refer to the wavefunction amplitude on sublattice A and B, respectively.

The Hamiltonian is proportional to the helicity operator $\frac{1}{2}\boldsymbol{\sigma} \cdot \boldsymbol{p}/|\boldsymbol{p}|$, *i.e.*, the projection of the pseudospin along the momentum direction, which is equivalent to the chirality for massless particles [1]. Therefore, the Dirac Hamiltonian obeys chiral symmetry, or in other words, free quasiparticles in graphene have a well-defined chirality with respect to their pseudospin. From the physical meaning of the pseudospin we can easily understand this abstract property as the symmetry

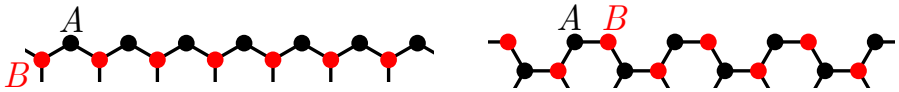

Figure 2.3.: Special types of graphene boundaries: Zigzag (left) and armchair (right). Sublattices A and B are represented by black and red dots, respectively.

between the two sublattices of the honeycomb lattice. For an infinite plane they are completely equivalent, but a disordered boundary will in general break this symmetry.

2.4. Graphene boundaries

In principle, there are arbitrarily many ways to terminate a graphene sheet. Due to the special lattice structure, there are however two special types of straight graphene edges which are called "zigzag" and "armchair" because of their characteristic shape. These two boundary types have quite different properties, *e.g.*, concerning the existence of localized edge states. In the tight-binding model, boundary conditions are implemented by demanding that the wavefunction amplitude has to vanish on the first lattice sites that are outside the lattice. For the zigzag boundary they all belong to the same sublattice B, as seen in Fig. 2.3. However, the wavefunction amplitude can be large on the sublattice A. For this reason, bound states that are localized on the boundary can exist. On an armchair edge both components of the wavefunction have to vanish on the boundary and edge states are not possible (cf. [1]).

It can be shown that within the Dirac approximation, *i.e.*, in the low-energy regime, any boundary conditions that do not cut along the armchair orientation are of zigzag type, hence the zigzag boundary condition is the generic one [10]. For this reason we will further on only consider boundaries of zigzag type.

3. Solving the scattering problem

The aim of this thesis is to study scattering at a single disordered edge of a semi-infinite graphene sample, first at the Dirac points, *i.e.*, at the Fermi energy of neutral graphene $E_F = 0$, and then also at finite doping $E_F > 0$, where we potentially have a large number of propagating modes that contribute to electronic transport. In particular, we would like to understand the strength of diffusive scattering at such a disordered boundary. As stated in the title, our main focus will be on the influence of chiral symmetry on diffusive scattering.

3.1. General idea

For a clean straight boundary we have purely specular reflection due to conservation of the momentum along the boundary, *i.e.*, an incoming mode with an angle ϑ_{in} with respect to the boundary normal is scattered with probability one into an outgoing mode with the same angle $\vartheta_{\text{out}} = -\vartheta_{\text{in}}$, where for consistency we define angles left of the surface normal to be negative and angles on the right to be positive (cf. Fig. 3.1). However, if we introduce some edge roughness, there will as well be diffusive contributions into different angles that will be responsible for a decrease of the conductance parallel to the edge. At the Dirac points, the notion of diffusive scattering is equivalent to the relation between inter- and intra-valley scattering, *i.e.*, scattering processes between and within the two distinct Dirac cones. If we only consider a single cone, we can even relate the "diffusiveness" to the distribution of the scattering phase that the mode acquires.

The discussion of diffusive scattering is always based on the analysis of the scattering matrix, as it contains all relevant information about scattering processes. In this chapter we will therefore discuss all steps necessary to solve the scattering problem for a disordered graphene boundary. We first define the system geometry that we consider throughout this thesis in Section 3.2. We proceed in Section 3.3 by describing two different approaches to model disorder on the boundary, starting from the continuum description of the Dirac equation and from the tight-binding approximation. In Chapter 2 they were shown to be equivalent formulations for the low-energy physics in graphene. Further, we will see in Section 3.4 how disorder can influence the chiral symmetry of graphene that will play a significant role for diffusive scattering. Having specified the system of interest, in Section 3.5 we give

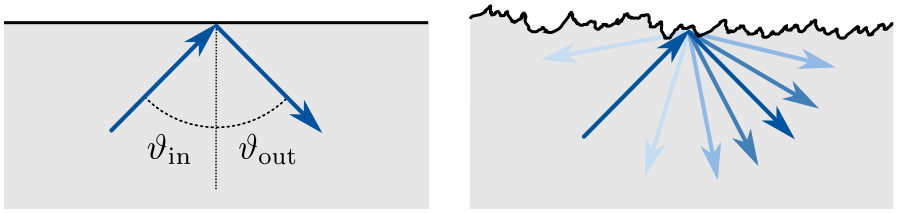

Figure 3.1.: Schematic view of scattering at a clean (left) and at a disordered boundary (right). The semi-infinite graphene sheet (gray) has a single boundary (black line) and is assumed to be continued infinitely in all other directions. Blue arrows indicate the paths of incoming and outgoing modes. For a clean boundary (left), the direction of motion of the outgoing mode is uniquely determined by that of the incoming mode. For a disordered boundary (right), there are many possible modes into which an incoming mode can scatter with different probabilities, indicated by different saturation of the arrows.

a definition of the scattering matrix and outline the general idea of how to solve the scattering problem and obtain the scattering matrix for a system as the one we are interested in. Moreover, the explicit structure of the scattering matrix for the case of scattering at the Dirac points will be specified. We will conclude this outline of the general ideas involved in this thesis by explaining the notion of self-averaging in Section 3.6, which is a central point of the scattering results obtained in Chapter 4.

3.2. Geometry of the system

Consider the following system (Fig. 3.2): A lead with translational invariance in y-direction is terminated by a disordered zigzag edge at $y = 0$ that will be specified below. Periodic boundary conditions in x-direction (parallel to the boundary, indicated by dotted lines) ensure that momentum is well-defined in this direction. In the limit of large lead width L we thereby model a semi-infinite plane with a single edge. As shown in Fig. 3.2, with this setup we basically roll up the semi-infinite sheet described above to a cylinder to better handle it mathematically. Technically, in this cylindrical picture (on the right in Fig. 3.2) the modes are now "approaching the boundary from below", meaning they come from $y = \infty$ and are scattered back to $y = \infty$ instead of going from left to right ($x = -\infty$ to $x = \infty$) in the nanoribbon picture explained in the beginning, which would intuitively be better reflected by the sketch on the left in Fig. 3.2. However, in the large-L limit these two pictures are completely equivalent.

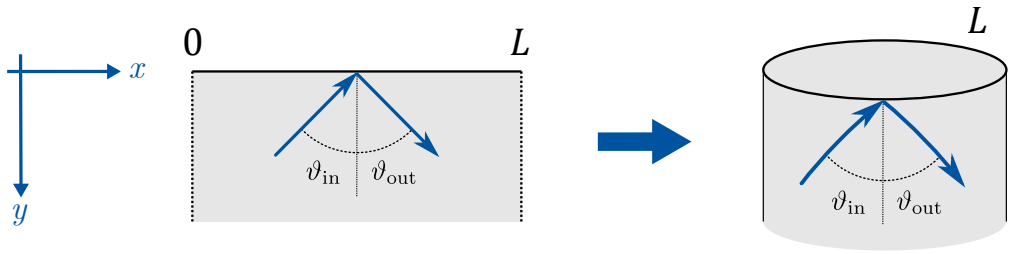

Figure 3.2.: Scheme of the system geometry: A graphene sheet (gray) with translational invariance in y-direction is terminated by a single boundary at $y = 0$. Applying periodic boundary conditions (left, dotted lines) in x-direction on the semi-infinite plane is equivalent to rolling it up to a cylinder (right). L is the boundary length after applying periodic boundary conditions. Blue arrows indicate schematically the paths of an incoming and an outgoing mode.

3.3. Modeling a disordered boundary

Let us now focus on the details of the boundary. There are different physical reasons why a real graphene edge will never be perfectly clean, but show some kind of disorder. Firstly, a graphene sample cannot be etched perfectly straight in experiment, thus edge roughness will be unavoidable. Furthermore, the outermost carbon atoms on a graphene edge only have two neighbors instead of three, therefore they have dangling bonds (unbound electrons) to which other atoms like hydrogen will attach. This so-called passivation can lead to a local shift in the chemical potential. All outermost atoms on a zigzag edge belong to the same sublattice, as it can be seen in Fig. 2.3. Hence, the passivation leads to a staggered potential on the boundary between sublattices A and B, which will be subject to spatial fluctuations.

Throughout the thesis, we will assume disorder to be caused by the latter effect. We will now discuss how we can describe such disorder in the two models that we will use to study electron scattering in our system. We start from the continuum description given by the Dirac equation, where we will even consider only a single valley of the graphene band structure. We then extend the consideration to the tight-binding model that lives on the actual honeycomb lattice.

3.3.1. Single-valley Dirac equation

Within the Dirac approximation, we completely omit the lattice and consider initially free Dirac fermions living on a 2D plane with the geometry discussed previously. The effect of a boundary terminating this plane in y-direction can

be achieved by introducing a confinement potential located where we want the boundary to be, as shown in [11], which translates into a linear restriction on the 4-spinor Dirac wavefunctions $\psi(x, y)$,

$$M\psi(x, y = 0) = \psi(x, y = 0)\,, \tag{3.3.1}$$

with a Hermitian unitary matrix M,

$$M = M^\dagger\,, \quad M^2 = \mathbb{1}\,. \tag{3.3.2}$$

The matrix M in this way fully specifies the properties of the boundary. In [10], all possible boundary conditions for Dirac fermions in graphene are discussed and classified. It is shown that in the valley-isotropic representation a clean zigzag boundary is represented by

$$M_{zz} = \tau_z \otimes \sigma_z\,. \tag{3.3.3}$$

A passivation of the outermost carbon atoms, *e.g.*, by hydrogen, affects on a zigzag boundary only atoms belonging to one sublattice and thereby creates a staggered potential between the sublattices A and B, as mentioned before (cf. [12]). It is shown in [10] that such a potential is represented by a boundary condition obtained by interpolating between a clean zigzag boundary M_{zz} and the Berry-Mondragon boundary condition [13]

$$M_{\mathrm{BM}} = \tau_z \otimes (\boldsymbol{\sigma} \cdot (\hat{\boldsymbol{z}} \times \boldsymbol{n}_B)) = \tau_z \otimes \sigma_x \tag{3.3.4}$$

for the boundary normal $\boldsymbol{n}_B = -\hat{\boldsymbol{y}}$. The Berry-Mondragon boundary condition is related to adding an infinitely large mass term located on the boundary to the Dirac equation, thereby creating a hard-wall boundary.

As both these boundary conditions are diagonal in valley space, any linear combination of them will as well not mix the valleys and we can reduce our consideration to just a single valley, such that we have

$$M_{zz} = \sigma_z\,, \quad M_{\mathrm{BM}} = \sigma_x \tag{3.3.5}$$

in the basis (ψ_A, ψ_B). To describe disorder induced by a spatially fluctuating staggered potential, we have to interpolate between these two boundary conditions by a random function $\theta(x)$ that depends on the position x on the boundary. Therefore we consider the boundary matrix

$$M = \cos\theta(x) M_{zz} + \sin\theta(x) M_{\mathrm{BM}} = \begin{pmatrix} \cos\theta(x) & \sin\theta(x) \\ \sin\theta(x) & -\cos\theta(x) \end{pmatrix}\,. \tag{3.3.6}$$

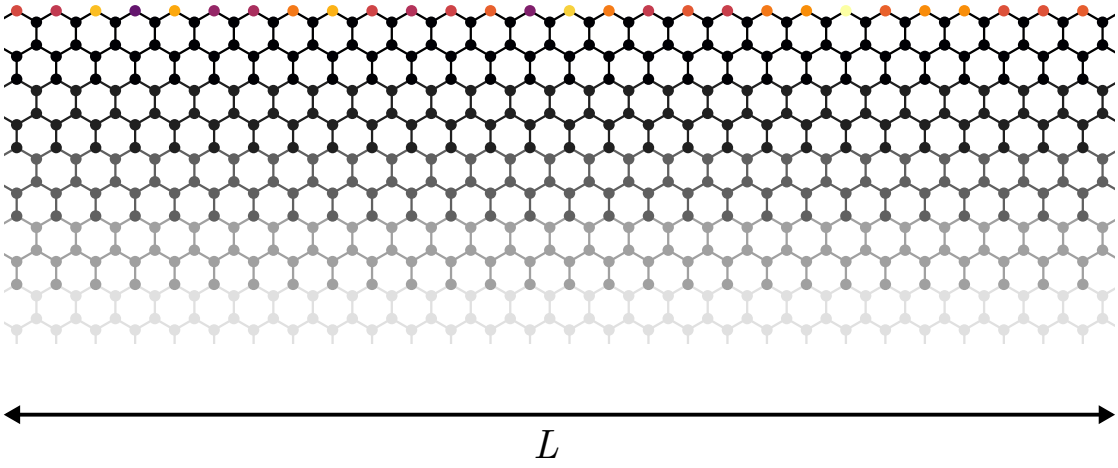

Figure 3.3.: Setup of the system within the tight-binding approach, with a zigzag edge of length L including onsite disorder on the outermost sites, represented by colored dots. Sites represented by black dots have zero onsite potential. The fading symbolizes infinite continuation in y-direction. Half hopping lines on the left and right are meant to be connected, thereby implementing periodic boundary conditions. The figure was created using *Kwant* [14].

For $\theta = 0$ we have a clean zigzag and for $\theta = \pi/2$ an infinite-mass boundary. The value of $\theta(x)$ at position x is a Gaussian distributed random variable with mean value θ_0 and standard deviation σ_θ. Here θ_0 indicates how strong the potential shift due to passivation is on average, and σ_θ is a measure of the strength of the disorder, as it tells how much the potential is fluctuating. The variables $\theta(x)$ and $\theta(x')$ are assumed to be uncorrelated for $x \neq x'$.

3.3.2. Tight-binding approach

Let us now consider the nearest-neighbor tight-binding model shown in Eq. (2.2.2) in Section 2.2,

$$H = -t \sum_{\langle i,j \rangle} |i\rangle\langle j| \,, \tag{3.3.7}$$

with a geometry as described before, shown in Fig. 3.3, the edge being of zigzag type. In this case the system is confined by simply omitting hoppings outside the system geometry, such that the sum in the Hamiltonian goes only over hoppings between sites within the system.

We will now include disorder on the boundary, motivated again by the effect of

passivation of the graphene edge. The local shift of the chemical potential on the boundary can be modeled by adding an onsite potential term

$$H_V = \sum_j V_j |j\rangle\langle j| \tag{3.3.8}$$

to the tight-binding model, which effectively shifts the chemical potential on the j-th lattice site from 0 to $-V_j$. We assume this effect to be subject to spatial random fluctuations. Therefore, we choose the V_j-s to be independent identically distributed Gaussian random variables with mean value V_0 and standard deviation V. The probability for V_j to take the value v_j is then given by

$$f_{V_j}(v_j) = \frac{1}{\sqrt{2\pi V^2}} e^{-(v_j - V_0)^2/2V^2} . \tag{3.3.9}$$

Correlations can be computed as

$$\langle V_i V_j \rangle = V^2 \delta_{ij} . \tag{3.3.10}$$

Hence potentials on different lattice sites are uncorrelated. From Eq. (3.3.10) we can understand V as the strength of the disorder: A larger value of V means higher fluctuations of the V_j and therefore a more disordered boundary. We apply the onsite potential term on the outermost sites j indicated by colored dots in Fig. 3.3; V_j is zero on all other sites j further away in the bulk (black dots).

3.4. Average chiral symmetry

In Chapter 2 we have learned that quasiparticles on an infinite graphene sheet obey a chiral symmetry that can be understood as the symmetry between the two sublattices of the honeycomb lattice. If we introduce disorder on the boundary, *e.g.*, by applying a disorder potential as explained in Section 3.3.2, we clearly break this symmetry between the sublattices A and B, as the outermost sites all belong to the same sublattice. However, if the mean value of the disorder potential V_0 is zero, an ensemble average over all possible disorder configurations suggests that *on average* a symmetry between the sublattices still remains. Only by setting V_0 to a finite value we would explicitly break the average chiral symmetry.

We can therefore study scattering with and without this average chiral symmetry by changing the average value of the disorder—θ_0 within the Dirac approach and V_0 in the tight-binding approximation—, and indeed we will see a significant qualitative difference between these two cases in the scattering results in Chapter 4.

3.5. Scattering matrix

Having specified the geometry of the system of interest and details of how to model its boundary, we can proceed to study scattering at this boundary. The most relevant quantity for this thesis is the scattering matrix S, since it contains all information about scattering processes. The matrix element S_{mn} is in general given by the scattering amplitude from an asymptotic incoming mode $|\psi_n^{\text{in}}\rangle$ to an outgoing mode $|\psi_m^{\text{out}}\rangle$. Hence, it tells us what happens to an electron that comes from infinity and reaches the scatterer (in our case the boundary) in a certain mode $|\psi_n^{\text{in}}\rangle$, with which probability it will be scattered into the mode $|\psi_m^{\text{out}}\rangle$ and which phase it will acquire during this scattering process.

We can solve the scattering problem and obtain the scattering matrix in three steps (see also in [15]): In the first step, we have to specify what we mean by asymptotic modes, and compute them explicitly. An electron coming from far away will not feel the boundary, therefore we can express incoming and outgoing states in the basis of eigenstates of the infinite lead obtained by omitting the boundary and continuing the lead also to $y = -\infty$. We therefore look for solutions to the Schrödinger equation

$$H_L^{\text{inf}}|\psi_L^{\text{inf}}\rangle = E|\psi_L^{\text{inf}}\rangle \tag{3.5.1}$$

for the infinite lead Hamiltonian H_L^{inf} at the energy E at which we want to solve the scattering problem. As the infinite lead has translational invariance in both x- and y-direction, these solutions will be given by Bloch waves. To distinguish incoming and outgoing modes, we have to rotate them into a basis in which the current operator in y-direction J_y is diagonal. Moreover, we have to normalize the rotated eigenstates properly such that they all have the same velocity v in y-direction to ensure that current is conserved on the boundary, *i.e.*, that the probability current of all incoming modes equals that of all outgoing modes. This condition is also necessary for S to be unitary as stated below. We then can write

$$\langle\psi_n^{\text{in}}|J_y|\psi_m^{\text{in}}\rangle = -v\delta_{nm}\,, \tag{3.5.2}$$

$$\langle\psi_n^{\text{out}}|J_y|\psi_m^{\text{out}}\rangle = +v\delta_{nm}\,, \tag{3.5.3}$$

$$\langle\psi_n^{\text{in}}|J_y|\psi_m^{\text{out}}\rangle = 0\,. \tag{3.5.4}$$

These states $\{|\psi_n^{\text{in}}\rangle\}$ and $\{|\psi_m^{\text{out}}\rangle\}$ form the bases in which we will express S. As we do not consider any magnetic fields, scattering will additionally obey time-reversal symmetry $\mathcal{T}$. We can thus order the bases of incoming and outgoing modes such that they reflect this symmetry via

$$(\psi_1^{\text{out}}, \psi_2^{\text{out}}, \dots) = \mathcal{T}(\psi_1^{\text{in}}, \psi_2^{\text{in}}, \dots)\,, \tag{3.5.5}$$

i.e., the outgoing modes being the time-reversed incoming ones. As we in fact do have a boundary and therefore restrict the system to positive y, we have to additionally allow for Bloch waves with imaginary momentum in y-direction, *i.e.*, evanescent modes $|\psi_n^{\mathrm{ev}}\rangle$ that decay exponentially for $y \to \infty$, which would not be normalizable on the infinite lead. Since we will eliminate these modes in the computation of S, their normalization is not relevant for the obtained result.

In a second step, we have to define and solve the scattering problem based on these modes. As we computed all possible eigenstates of the semi-infinite lead, it is clear that they form a complete basis of the lead Hilbert space, such that we can write any state living on the semi-infinite lead as

$$|\tilde{\psi}^L\rangle = \sum_m c_m^{\mathrm{in}} |\psi_m^{\mathrm{in}}\rangle + \sum_m c_m^{\mathrm{out}} |\psi_m^{\mathrm{out}}\rangle + \sum_m c_m^{\mathrm{ev}} |\psi_m^{\mathrm{ev}}\rangle \,, \tag{3.5.6}$$

with some complex coefficients c_m^{in}, c_m^{out}, c_m^{ev}. We are interested in what happens if a well-defined incoming state reaches the boundary. We therefore construct a scattering state $|\psi_n^L\rangle$ on the lead for each incoming mode $|\psi_n^{\mathrm{in}}\rangle$ where all coefficients c_m^{in} are zero for $m \neq n$:

$$|\psi_n^L\rangle = |\psi_n^{\mathrm{in}}\rangle + \sum_m |\psi_m^{\mathrm{out}}\rangle S_{mn} + \sum_m |\psi_m^{\mathrm{ev}}\rangle S_{mn}^{\mathrm{ev}} \,. \tag{3.5.7}$$

This representation shows the scattering process in a very physical way: The total lead wavefunction is a superposition of an incoming mode plus outgoing modes, weighted by the corresponding amplitudes to scatter into them, which is exactly where the coefficients of the scattering matrix come into play. Additionally one can excite evanescent modes with probability amplitudes S_{mn}^{ev}. The scattering states have to be solutions of the Schrödinger equation

$$H(|\psi_n^L\rangle \oplus |\psi_n^B\rangle) = E(|\psi_n^L\rangle \oplus |\psi_n^B\rangle) \tag{3.5.8}$$

for the full Hamiltonian H, including the description of the boundary, at the energy E. Here $|\psi_n^B\rangle$ describes the part of the scattering state living on the boundary for the incoming mode $|\psi_n^{\mathrm{in}}\rangle$. This constitutes a system of equations from which we can eliminate $|\psi_n^B\rangle$ and S^{ev} to finally solve it for S. In the Dirac approach we can simply use the boundary condition equation (3.3.1) applied on $|\psi_n^L\rangle$ to obtain a system of equations that we can solve for S.

In both approaches we have therefore reduced the scattering problem to a linear system of equations. By solving these equations we will obtain S as a function of the disorder, *i.e.*, as a function of $\theta(x)$ or of all V_j, respectively. Since we are not interested in the behavior for a specific configuration of the interpolation function $\theta(x)$ or the disorder potential, in a third and last step we have to average over

all possible disorder configurations (using the known distribution of, *e.g.*, V_j on a specific site). Thereby we eventually obtain the mean value and standard deviation

$$\langle S_{mn}\rangle = \begin{cases} \langle S_{mn}\rangle(\theta_0,\sigma_\theta)\,, & \text{(Dirac eq.)} \\ \langle S_{mn}\rangle(V_0,V)\,, & \text{(tight-binding)} \end{cases} \tag{3.5.9}$$

$$\sigma(S_{mn}) = \sqrt{\langle S_{mn}^2\rangle - \langle S_{mn}\rangle^2} = \begin{cases} \sigma(S_{mn})(\theta_0,\sigma_\theta)\,, & \text{(Dirac eq.)} \\ \sigma(S_{mn})(V_0,V)\,, & \text{(tight-binding)} \end{cases} \tag{3.5.10}$$

of elements S_{mn} of the scattering matrix as functions of the mean value of the disorder (θ_0 or V_0) and its standard deviation σ_θ or V that represents the disorder strength.

The scattering matrix has two important properties: Due to probability current conservation at the boundary (the probabilities to scatter into any outgoing mode have to sum up to one) S has to be unitary, fulfilling

$$SS^\dagger = \mathbb{1}\,. \tag{3.5.11}$$

This very general property requires the modes to be properly current normalized as emphasized previously. Furthermore, as stated before, our system is invariant under time-reversal. One can show that as a result, within the basis chosen to reflect this symmetry, S has as well to be symmetric with

$$S = S^T\,. \tag{3.5.12}$$

3.5.1. Structure of the scattering matrix at the Dirac points

In Chapter 4 we will solve the scattering problem at the Fermi energy of neutral graphene $E_F = 0$. The Fermi energy then lies exactly at the Dirac points. The Fermi "surface" thus only consists of the Dirac points, and the cylindrical lead has only four propagating eigenstates at this energy: One from the upper and one from the lower cone, for each Dirac point. By going into the eigenbasis of the current operator normal to the boundary, we obtain two incoming and two outgoing modes (one incoming and one outgoing for each valley). Therefore, the scattering matrix is of size 2×2. We choose the basis of the incoming modes as $(\psi^{\text{in}}_{\boldsymbol{K}}, \psi^{\text{in}}_{\boldsymbol{K}'})$ and that of the outgoing ones as $(\psi^{\text{out}}_{\boldsymbol{K}'}, \psi^{\text{out}}_{\boldsymbol{K}}) = \mathcal{T}(\psi^{\text{in}}_{\boldsymbol{K}}, \psi^{\text{in}}_{\boldsymbol{K}'})$, *i.e.*, the outgoing modes to be the time-reversed incoming modes. Assuming S to be unitary and symmetric (Eqs. (3.5.11), (3.5.12)), we can parametrize it as

$$S = e^{i\phi}\begin{pmatrix} re^{i\Delta} & \sqrt{1-r^2} \\ \sqrt{1-r^2} & -re^{-i\Delta} \end{pmatrix}\,, \tag{3.5.13}$$

which is shown in Appendix A.

Hence we remain with three free parameters to compute,

- the inter-valley scattering amplitude r (r^2 is the probability to scatter into the other cone),
- the intra-valley scattering phase ϕ that is acquired when scattering within one cone, and
- a relative phase Δ between inter- and intra-valley scattering that is however completely random and uniformly distributed over $[0, 2\pi)$ (as we see from numerics), which can be easily understood from the fact that it is not fixed even for a clean zigzag boundary (see Eq. (3.5.14)).

For pure specular reflection, *i.e.*, scattering only from $\boldsymbol{K}$ to $\boldsymbol{K}$ and from $\boldsymbol{K'}$ to $\boldsymbol{K'}$, acquiring a fixed constant phase ϕ_0, the scattering matrix is given by

$$S = e^{i\phi_0} \begin{pmatrix} 0 & 1 \\ 1 & 0 \end{pmatrix} , \tag{3.5.14}$$

with $\phi_0 = 0$ for a clean zigzag boundary. Hence for $E_F = 0$ the notion of "diffusiveness" that comes into play when including disorder is captured by just these parameters r^2 and ϕ, *i.e.*, by the relative amount of scattering between the cones and by fluctuations of the scattering phase that are caused by the disorder.

In the single-cone approximation used in the Dirac approach in Section 4.1, we even neglect inter-valley scattering ($r = 0$) as mentioned before and project onto the $\boldsymbol{K}$-point, remaining with one incoming and one outgoing mode and just a scattering phase

$$S = e^{i\phi} . \tag{3.5.15}$$

In this case the amount of diffusiveness is described solely by the distribution of ϕ; if ϕ is constant we call scattering specular.

3.6. Self-averaging

As mentioned in the beginning, to help our intuition we can always think of light scattering at disordered surfaces as a classical analogon to electron scattering at disordered graphene boundaries. A standard everyday application where diffusive scattering is effectively reduced is a mirror. A mirror will—as we know from our everyday experience—reflect all incoming light specularly such that we can clearly see ourselves in it. However, its surface can never be polished perfectly and will therefore still have some surface roughness on a microscopic scale, which from a

naïve point of view should produce a significant amount of diffusive scattering, making a clear mirror image impossible. The explanation of this phenomenon is based on the relevant length scales: The typical scale of the roughness is much smaller than the wavelengths of visible light, therefore diffusive contributions average out and are thereby effectively suppressed.

A similar behavior should be observable for our model as well: In the large-Fermi wavelength limit we would expect a suppression of diffusive contributions, leaving us with mainly (or purely) specular reflection. As the Fermi wavelength $\lambda_F \propto 1/E_F$ (Eq. (2.2.9)), for scattering at the Dirac points ($E_F = 0$) the Fermi wavelength is already infinite, such that the boundary length L plays the role of the relevant length scale over which self-averaging can happen. A major point of interest will therefore be the large-L behavior, in which we expect our system to resemble a clean boundary for sufficiently weak disorder.

3.7. Conclusion

In this chapter it was shown how we model disordered boundaries in the Dirac and the tight-binding approach, and how we can reduce the scattering problem to a linear system of equations that we can solve for the scattering matrix of such a boundary. We have also seen that at the Dirac points the scattering matrix can essentially be expressed by just two parameters that we can very physically interpret as the probability to scatter between the two Dirac cones and the scattering phase a mode acquires. In the next chapter we will explicitly compute the scattering phase from the Dirac equation and both parameters in the tight-binding approach to study their dependence on the disorder strength and, more importantly, on its average value that we have identified to be closely related to the chiral symmetry.

4. Scattering at the Dirac points

In this chapter we study scattering at the Dirac points, *i.e.*, at a Fermi energy $E_F = 0$, within the two approaches introduced in Section 3.3, the Dirac-equation for a single valley and the tight-binding approximation. Within the low-energy regime and for disorder that does not mix the valleys as discussed in Section 3.3.1, these approaches are equivalent descriptions of graphene physics. Starting with the Dirac continuum description for only a single valley to understand "diffusiveness" in terms of the distribution of the scattering phase, we will then proceed with the tight-binding approach to study disorder that also induces inter-valley scattering. We compute the scattering matrix analytically in both approaches and discuss the results for broken and preserved chiral symmetry.

4.1. Single-valley Dirac equation

The procedure to obtain the scattering phase from the Dirac equation is as outlined in Section 3.5. In Section 4.1.1 the model Hamiltonian is shown and propagating and evanescent eigenmodes of the lead are computed. We continue in Section 4.1.2 by introducing disorder via an appropriate boundary condition, which constitutes a system of equations that we can solve for the scattering phase. In Section 4.1.3 we will study how chiral symmetry distinguishes two limits of the resulting scattering phase. The scattering results within these limits of broken and preserved chiral symmetry will be discussed in Sections 4.1.4 and 4.1.5.

4.1.1. Hamiltonian and eigenstates

We start from the Dirac Hamiltonian (Eq. (2.3.1))

$$H = v_F \tau_0 \otimes (\boldsymbol{\sigma} \cdot \boldsymbol{p}) \,. \tag{4.1.1}$$

As discussed in Section 3.3.1, the boundary condition that we will use to describe a disordered boundary does not mix the two valleys. Hence, it is sufficient to consider only a single cone and project H onto the $\boldsymbol{K}$-subspace, such that we

remain with

$$H = v_F\,\boldsymbol{\sigma}\cdot\boldsymbol{p} = -i\hbar v_F \begin{pmatrix} & \partial_x - i\partial_y \\ \partial_x + i\partial_y & \end{pmatrix} . \tag{4.1.2}$$

With the ansatz

$$\psi(\boldsymbol{r}) = e^{i\boldsymbol{q}\cdot\boldsymbol{r}} \begin{pmatrix} \psi_A \\ \psi_B \end{pmatrix} \tag{4.1.3}$$

we obtain from the Dirac equation at zero energy $H\psi = 0$

$$\begin{cases} (q_x - iq_y)\psi_B = 0\,, \\ (q_x + iq_y)\psi_A = 0\,. \end{cases} \tag{4.1.4}$$

Periodic boundary conditions in x-direction restrict the momentum q_x as

$$\psi(x,y) = \psi(x+L,y) \quad \Rightarrow \quad q_x = \frac{2\pi}{L}n\,, \quad n \in \mathbb{Z}\,. \tag{4.1.5}$$

Assuming the boundary at $y = 0$ and the graphene sheet to extend to positive y as defined in Section 3.2, we can write down all non-trivial solutions of Eq. (4.1.4) for given n. We can distinguish two cases, depending on the behavior for $y \to \infty$.

Propagating modes: For $n = 0$ we have $\boldsymbol{q} = 0$ and therefore all states $\psi = (\psi_A, \psi_B)^T$ are solutions to the Dirac equation (4.1.4). We can choose an orthonormal basis $\{\psi_+, \psi_-\}$ of that two-dimensional subspace that diagonalizes the y-component of the current operator $\boldsymbol{J} = v_F\boldsymbol{\sigma}$ [10], such that $\psi_\pm$ have well-defined current $\pm v_F$ perpendicular to the boundary,

$$\psi_\eta^\dagger J_y \psi_\nu = \eta v_F \delta_{\eta\nu}\,, \quad \eta,\nu = \pm\,, \tag{4.1.6}$$

$$\psi_\eta^\dagger \psi_\nu = \delta_{\eta\nu}\,. \tag{4.1.7}$$

The propagating modes are therefore the eigenstates of σ_y that can be written as

$$\psi_\pm(x,y) = \frac{1}{\sqrt{2}} \begin{pmatrix} 1 \\ \pm i \end{pmatrix} . \tag{4.1.8}$$

As ψ_- has a velocity $-v_F$ and is thus moving in negative y-direction, we consider it to be incoming and ψ_+ to be outgoing, respectively.

Evanescent modes: For $n \neq 0$ the Dirac equation (4.1.4) becomes

$$\begin{cases} \left(\frac{2\pi}{L}\, n - iq_y\right) \psi_B = 0\,, \\ \left(\frac{2\pi}{L}\, n + iq_y\right) \psi_A = 0\,. \end{cases} \tag{4.1.9}$$

such that we get two non-trivial solutions for each n:

- $q_y = -\frac{2\pi i}{L} n$ and $\psi_A = 0 \quad \Rightarrow \quad \psi_{n,-}(x,y) = e^{2\pi i n x/L} e^{2\pi n y/L} \begin{pmatrix} 0 \\ 1 \end{pmatrix}$.

  This mode decays exponentially into the bulk for $y \to \infty$ if $n < 0$, but is not normalizable for positive y if $n > 0$.

- $q_y = \frac{2\pi i}{L} n$ and $\psi_B = 0 \quad \Rightarrow \quad \psi_{n,+}(x,y) = e^{2\pi i n x/L} e^{-2\pi n y/L} \begin{pmatrix} 1 \\ 0 \end{pmatrix}$.

  This mode is evanescent if $n > 0$, but not normalizable if $n < 0$.

In total we thus remain with one evanescent mode for each $n \in \mathbb{Z} \setminus \{0\}$.

4.1.2. Computation of the scattering phase

As stated in Section 3.5, we can now construct a scattering state ψ from the incoming mode ψ_-, outgoing mode ψ_+ and evanescent modes $\psi_{n,\pm}$ as

$$\psi = \psi_- + S\psi_+ + \sum_{n=1}^{\infty} (\alpha_n \psi_{n,+} + \alpha_{-n} \psi_{-n,-})\,, \tag{4.1.10}$$

where S is the "scattering matrix" (in this case just a scattering phase $S = e^{i\phi}$) and α_n is the amplitude to scatter into the n-th evanescent mode.

As explained in Section 2.3, a boundary is introduced by requiring this scattering state to fulfill the boundary condition given by Eq. (3.3.1), where the boundary matrix M defined in Eq. (3.3.6) introduces disorder through the function $\theta(x)$. With $\psi(x, y = 0) = (\psi_A(x), \psi_B(x))^T$ we obtain

$$\begin{aligned} &\begin{pmatrix} \cos\theta(x) - 1 & \sin\theta(x) \\ \sin\theta(x) & -\cos\theta(x) - 1 \end{pmatrix} \begin{pmatrix} \psi_A(x) \\ \psi_B(x) \end{pmatrix} = 0 \\ \Rightarrow &\begin{pmatrix} \tan(\theta(x)/2) & -1 \\ -1 & 1/\tan(\theta(x)/2) \end{pmatrix} \begin{pmatrix} \psi_A(x) \\ \psi_B(x) \end{pmatrix} = 0\,, \end{aligned} \tag{4.1.11}$$

from which we get

$$\mu(x)\sum_{n=0}^{\infty}\alpha_n e^{2\pi inx/L} = i(\alpha_0-\sqrt{2}) + \sum_{n=1}^{\infty}\alpha_{-n}e^{-2\pi inx/L}\,, \tag{4.1.12}$$

where

$$\mu(x) = \tan(\theta(x)/2) \tag{4.1.13}$$

is 0 for a clean zigzag and 1 for the infinite-mass type boundary, and

$$\alpha_0 = (1+S)/\sqrt{2}\,. \tag{4.1.14}$$

The boundary condition Eq. (4.1.12) depends on infinitely many evanescent modes. However, the evanescent modes $\psi_{n,\pm}$ decay on a length scale $L/2\pi|n|$ decreasing with $|n|$, and as the real problem lives on a lattice, modes which decay on a scale smaller than the lattice constant will not play an important role. We therefore introduce a momentum cutoff N (which we eventually can put to infinity again) such that $\alpha_n = 0$ for $|n| > N$. Correspondingly, we discretize the x-axis by introducing a lattice constant a, $x_m = ma$, with $m = 0,\ldots,2N$ and $a = \frac{L}{2N+1}$, as we remain with $2N$ evanescent and 1 (outgoing) propagating mode to scatter into. The boundary condition Eq. (4.1.12) then reads

$$\sum_{n=0}^{N}\mu_m e^{2\pi imn/(2N+1)}\alpha_n - \sum_{n=1}^{N}e^{-2\pi imn/(2N+1)}\alpha_{-n} - i\alpha_0 = -i\sqrt{2}\,,\quad m=0,\ldots,2N\,, \tag{4.1.15}$$

with $\mu_m = \mu(x_m)$. We can write this system of equations as

$$\sum_{n=-N}^{N}A_{mn}\alpha_n = -i\sqrt{2}\,, \tag{4.1.16}$$

with

$$A_{mn} = \Big[\mu_m\Theta(n) - \Theta(-n) + (1-i)\delta_{n,0}\Big]e^{2\pi imn/(2N+1)}\,, \tag{4.1.17}$$

where we define the discrete Heaviside function as

$$\Theta(n) = \begin{cases}1,\ n\geq 0\,,\\ 0,\ n<0\,.\end{cases} \tag{4.1.18}$$

The exponential factor in A_{mn} suggests to apply a discrete Fourier transform by

multiplying both sides of Eq. (4.1.16) by $U^\dagger$, with

$$U_{mn} = \frac{1}{\sqrt{2N+1}}\, e^{2\pi i mn/(2N+1)}\,. \tag{4.1.19}$$

On the left hand side of Eq. (4.1.16) we evaluate

$$\sum_{m=0}^{2N} U^\dagger_{km} A_{mn} = \tilde{\mu}_{n-k}\Theta(n) + \sqrt{2N+1}\Big[-\Theta(-n) + (1-i)\delta_{n,0}\Big]\delta_{k,n} \tag{4.1.20}$$

and on the right hand side

$$\sum_{m=0}^{2N} U^\dagger_{km}(-i\sqrt{2}) = -i\sqrt{2}\,\sqrt{2N+1}\,\delta_{k,0}\,, \tag{4.1.21}$$

for $k = 0, \ldots, 2N$. Here we introduce the Fourier coefficients of the disorder function μ,

$$\tilde{\mu}_k = \frac{1}{\sqrt{2N+1}} \sum_{m=0}^{2N} \mu_m e^{2\pi i mk/(2N+1)}\,. \tag{4.1.22}$$

We can then write the Fourier transform of Eq. (4.1.16) in matrix form as

$$\tilde{\boldsymbol{A}}\boldsymbol{\alpha} = \boldsymbol{v}\,, \tag{4.1.23}$$

where, if we resort the α_n as $\boldsymbol{\alpha} = (\alpha_0, \alpha_1, \ldots, \alpha_N, \alpha_{-N}, \ldots, \alpha_{-1})^T$,

$$\tilde{\boldsymbol{A}} = \left(\begin{array}{c|cc} \tilde{\nu}_0 & \tilde{\mu}^\dagger_\downarrow & 0 \\ \hline \tilde{\mu}_\downarrow & \tilde{\boldsymbol{\mu}} & 0 \\ \tilde{\mu}_\uparrow & \tilde{\boldsymbol{\mu}}' & -\sqrt{2N+1}\;\mathbb{1}_N \end{array}\right)\,, \quad \boldsymbol{v} = -i\sqrt{2}\,\sqrt{2N+1}\begin{pmatrix} 1 \\ 0 \\ \vdots \\ 0 \end{pmatrix}\,, \tag{4.1.24}$$

with

$$\tilde{\nu}_0 = \tilde{\mu}_0 - i\sqrt{2N+1}\,, \quad \tilde{\mu}_\uparrow = \begin{pmatrix} \tilde{\mu}_N \\ \vdots \\ \tilde{\mu}_1 \end{pmatrix}\,, \quad \tilde{\mu}_\downarrow = \begin{pmatrix} \tilde{\mu}_{-1} \\ \vdots \\ \tilde{\mu}_{-N} \end{pmatrix} = \begin{pmatrix} \tilde{\mu}^*_1 \\ \vdots \\ \tilde{\mu}^*_N \end{pmatrix}\,,$$

$$\tilde{\boldsymbol{\mu}} = \begin{pmatrix} \tilde{\mu}_0 & \cdots & \tilde{\mu}_{N-1} \\ \vdots & \ddots & \vdots \\ \tilde{\mu}^*_{N-1} & \cdots & \tilde{\mu}_0 \end{pmatrix}\,, \quad \tilde{\boldsymbol{\mu}}' = \begin{pmatrix} \tilde{\mu}_{N+1} & \cdots & \tilde{\mu}_{2N} \\ \vdots & \ddots & \vdots \\ \tilde{\mu}_2 & \cdots & \tilde{\mu}_{N+1} \end{pmatrix}\,. \tag{4.1.25}$$

Hence, we have transformed the general boundary condition (Eq. (3.3.1)) into a system of equations for the scattering phase (expressed through α_0). This system is specified by the Fourier coefficients of the disorder function μ. To solve Eq. (4.1.23) for S, we have to invert $\tilde{\boldsymbol{A}}$, as

$$\boldsymbol{\alpha} = \tilde{\boldsymbol{A}}^{-1}\boldsymbol{v} \quad \Rightarrow \quad S = \sqrt{2}\alpha_0 - 1 = -1 - 2i\sqrt{2N+1}\,(\tilde{\boldsymbol{A}}^{-1})_{0,0}\,. \tag{4.1.26}$$

Quadratic matrices of the form $\begin{pmatrix} A & B \\ C & D \end{pmatrix}$ with arbitrary blocks A, B, C, and D (that not necessarily have to have the same dimensions), can be inverted using the general block matrix inversion formula

$$\begin{pmatrix} A & B \\ C & D \end{pmatrix}^{-1} = \begin{pmatrix} A^{-1} + A^{-1}B(D-CA^{-1}B)^{-1}CA^{-1} & -A^{-1}B(D-CA^{-1}B)^{-1} \\ -(D-CA^{-1}B)^{-1}CA^{-1} & (D-CA^{-1}B)^{-1} \end{pmatrix}. \tag{4.1.27}$$

This equality holds true if A and its so-called Schur complement $D - CA^{-1}B$ are invertible. We only need to compute the (0,0)-component (upper left component) of $\tilde{\boldsymbol{A}}^{-1}$. Thus, we can use this formula with $A = \tilde{\nu}_0$, assuming $\tilde{\nu}_0$ and its Schur complement in $\tilde{\boldsymbol{A}}$ to be invertible, to obtain

$$\begin{aligned}(\tilde{\boldsymbol{A}}^{-1})_{0,0} &= \frac{1}{\tilde{\nu}_0} + \frac{1}{\tilde{\nu}_0}\begin{pmatrix}\tilde{\mu}_\downarrow^\dagger & 0\end{pmatrix}\left[\begin{pmatrix}\tilde{\boldsymbol{\mu}} & 0 \\ \tilde{\boldsymbol{\mu}}' & -\sqrt{2N+1}\,\mathbb{1}\end{pmatrix} - \begin{pmatrix}\tilde{\mu}_\downarrow \\ \tilde{\mu}_\uparrow\end{pmatrix}\frac{1}{\tilde{\nu}_0}\begin{pmatrix}\tilde{\mu}_\downarrow^\dagger & 0\end{pmatrix}\right]^{-1}\begin{pmatrix}\tilde{\mu}_\downarrow \\ \tilde{\mu}_\uparrow\end{pmatrix}\frac{1}{\tilde{\nu}_0} \\ &= \frac{1}{\tilde{\nu}_0} + \frac{1}{\tilde{\nu}_0^2}\begin{pmatrix}\tilde{\mu}_\downarrow^\dagger & 0\end{pmatrix}\left[\begin{pmatrix}\tilde{\boldsymbol{\mu}} - \frac{\tilde{\mu}_\downarrow\tilde{\mu}_\downarrow^\dagger}{\tilde{\nu}_0} & 0 \\ \tilde{\boldsymbol{\mu}}' - \frac{\tilde{\mu}_\uparrow\tilde{\mu}_\downarrow^\dagger}{\tilde{\nu}_0} & -\sqrt{2N+1}\,\mathbb{1}\end{pmatrix}\right]^{-1}\begin{pmatrix}\tilde{\mu}_\downarrow \\ \tilde{\mu}_\uparrow\end{pmatrix}.\end{aligned} \tag{4.1.28}$$

Assuming the invertibility of $\tilde{\boldsymbol{\mu}} - \tilde{\mu}_\downarrow\tilde{\mu}_\downarrow^\dagger/\tilde{\nu}_0$, we can use Eq. (4.1.27) again to invert the matrix in square brackets. We get

$$\begin{aligned}(\tilde{\boldsymbol{A}}^{-1})_{0,0} &= \frac{1}{\tilde{\nu}_0} + \frac{1}{\tilde{\nu}_0^2}\begin{pmatrix}\tilde{\mu}_\downarrow^\dagger & 0\end{pmatrix}\begin{pmatrix}\left[\tilde{\boldsymbol{\mu}} - \frac{\tilde{\mu}_\downarrow\tilde{\mu}_\downarrow^\dagger}{\tilde{\nu}_0}\right]^{-1} & 0 \\ -\left[\tilde{\boldsymbol{\mu}} - \frac{\tilde{\mu}_\downarrow\tilde{\mu}_\downarrow^\dagger}{\tilde{\nu}_0}\right]^{-1}\left(\tilde{\boldsymbol{\mu}}' - \frac{\tilde{\mu}_\uparrow\tilde{\mu}_\downarrow^\dagger}{\tilde{\nu}_0}\right) & -\frac{1}{\sqrt{2N+1}}\,\mathbb{1}\end{pmatrix}\begin{pmatrix}\tilde{\mu}_\downarrow \\ \tilde{\mu}_\uparrow\end{pmatrix} \\ &= \frac{1}{\tilde{\nu}_0} + \frac{1}{\tilde{\nu}_0^2}\,\tilde{\mu}_\downarrow^\dagger\left[\tilde{\boldsymbol{\mu}} - \frac{\tilde{\mu}_\downarrow\tilde{\mu}_\downarrow^\dagger}{\tilde{\nu}_0}\right]^{-1}\tilde{\mu}_\downarrow\,.\end{aligned} \tag{4.1.29}$$

The product $\tilde{\mu}_\downarrow\tilde{\mu}_\downarrow^\dagger/\tilde{\nu}_0$ is a rank-1 update to $\tilde{\boldsymbol{\mu}}$. Therefore, one can use the Sherman-

Morrison-Woodbury formula [16] for invertible A and column vectors u, v,

$$\left(A - uv^T\right)^{-1} = A^{-1} + \frac{A^{-1}uv^TA^{-1}}{1 - v^TA^{-1}u}\,, \tag{4.1.30}$$

to finally obtain

$$\begin{aligned}(\tilde{\boldsymbol{A}}^{-1})_{0,0} &= \frac{1}{\tilde{\nu}_0} + \frac{1}{\tilde{\nu}_0^2}\left(\tilde{\mu}_\downarrow^\dagger\tilde{\boldsymbol{\mu}}^{-1}\tilde{\mu}_\downarrow + \frac{\frac{1}{\tilde{\nu}_0}\tilde{\mu}_\downarrow^\dagger\tilde{\boldsymbol{\mu}}^{-1}\tilde{\mu}_\downarrow\tilde{\mu}_\downarrow^\dagger\tilde{\boldsymbol{\mu}}^{-1}\tilde{\mu}_\downarrow}{1 - \frac{1}{\tilde{\nu}_0}\tilde{\mu}_\downarrow^\dagger\tilde{\boldsymbol{\mu}}^{-1}\tilde{\mu}_\downarrow}\right) \\ &= \frac{1}{\tilde{\nu}_0}\left(1 + \frac{\tilde{\nu}}{\tilde{\nu}_0} + \frac{(\frac{\tilde{\nu}}{\tilde{\nu}_0})^2}{1 - \frac{\tilde{\nu}}{\tilde{\nu}_0}}\right)\,,\end{aligned} \tag{4.1.31}$$

with

$$\tilde{\nu} = \tilde{\mu}_\downarrow^\dagger\tilde{\boldsymbol{\mu}}^{-1}\tilde{\mu}_\downarrow\,. \tag{4.1.32}$$

Thus, we can write the scattering matrix with Eq. (4.1.26) as

$$S = -1 + \frac{2}{\tilde{m}_0}\left(1 + i\frac{\tilde{m}}{\tilde{m}_0} - \frac{\left(\frac{\tilde{m}}{\tilde{m}_0}\right)^2}{1 - i\frac{\tilde{m}}{\tilde{m}_0}}\right)\,, \tag{4.1.33}$$

where

$$\tilde{m}_0 = \frac{i\tilde{\nu}_0}{\sqrt{2N+1}} = 1 + \frac{i\tilde{\mu}_0}{\sqrt{2N+1}}\,, \quad \tilde{m} = \frac{\tilde{\nu}}{\sqrt{2N+1}} = \frac{\tilde{\mu}_\downarrow^\dagger\tilde{\boldsymbol{\mu}}^{-1}\tilde{\mu}_\downarrow}{\sqrt{2N+1}}\,. \tag{4.1.34}$$

4.1.3. Implementation of chiral symmetry

As pointed out in Section 3.5, we are not interested in any specific configuration of the disorder potential, but we want to make statements about an average behavior of the scattering phase ϕ as a function of the mean value θ_0 and fluctuations σ_θ of the interpolation function $\theta(x_m)$ that incorporates disorder on the boundary. Therefore, it is necessary to average the above expressions over all $\theta(x_m)$ or $\tilde{\mu}_k$, respectively. However, these expressions include the inverse of the matrix

$$\tilde{\boldsymbol{\mu}} = \begin{pmatrix} \tilde{\mu}_0 & \cdots & \tilde{\mu}_{N-1} \\ \vdots & \ddots & \vdots \\ \tilde{\mu}_{N-1}^* & \cdots & \tilde{\mu}_0 \end{pmatrix}\,. \tag{4.1.35}$$

This is a so-called Toeplitz matrix, as it has constant values on all diagonals, and moreover, it is Hermitian. There are many algorithms known to efficiently invert Toeplitz matrices numerically for fixed N (*e.g.*, [17]). However, an explicit analytical inversion depending on N seems in general not to be possible, if no further assumptions on the $\tilde{\mu}_k$ are made.

Nevertheless, we can learn more about $\tilde{\boldsymbol{\mu}}^{-1}$ if we take a closer look onto the structure of the $\tilde{\mu}_k$. Let us therefore decompose the interpolation parameter $\theta(x_m)$ into a constant mean value θ_0 and fluctuations $\delta\theta(x_m) = \delta\theta_m$ with

$$\theta(x_m) = \theta_0 + \delta\theta_m \,, \tag{4.1.36}$$

$$\langle \delta\theta_m \rangle = 0 \,, \tag{4.1.37}$$

$$\langle \delta\theta_m \delta\theta_n \rangle = \sigma_\theta^2 \, \delta_{mn} \,. \tag{4.1.38}$$

Assuming the disorder to be weak, $\sigma_\theta \ll 1$, we can also expand $\mu(x) = \tan(\theta(x)/2)$ to get

$$\begin{aligned} \mu_m = \mu(x_m) = \tan\left(\frac{\theta_0 + \delta\theta_m}{2}\right) &= \tan\left(\frac{\theta_0}{2}\right) + \frac{1 + \tan^2\left(\frac{\theta_0}{2}\right)}{2} \, \delta\theta_m + \mathcal{O}\left(\delta\theta_m^2\right) \\ &= \mu_0 + \delta\mu_m + \mathcal{O}\left(\delta\mu_m^2\right) \,. \end{aligned} \tag{4.1.39}$$

We obtain after Fourier transforming

$$\tilde{\mu}_k = \frac{1}{\sqrt{2N+1}} \sum_{m=0}^{2N} (\mu_0 + \delta\mu_m) e^{2\pi i m k/(2N+1)} = \sqrt{2N+1} \, \mu_0 \, \delta_{k,0} + \sigma_\mu \tilde{x}_k \tag{4.1.40}$$

where

$$\sigma_\mu = \frac{1 + \tan^2\left(\frac{\theta_0}{2}\right)}{2} \, \sigma_\theta \tag{4.1.41}$$

is the standard deviation of μ and

$$\tilde{x}_k = \frac{1}{\sigma_\mu \sqrt{2N+1}} \sum_m \delta\mu_m e^{2\pi i m k/(2N+1)} \tag{4.1.42}$$

is normalized to have standard deviation 1 and by definition a mean value of 0. With Eq. (4.1.40) we get

$$\tilde{\boldsymbol{\mu}} = \sqrt{2N+1} \, \mu_0 \, \mathbb{1}_N + \sigma_\mu \tilde{\boldsymbol{x}} \,, \tag{4.1.43}$$

thereby splitting it up into a diagonal part which is trivial to invert and a random

Toeplitz matrix

$$\tilde{\boldsymbol{x}} = \begin{pmatrix} \tilde{x}_0 & \dots & \tilde{x}_{N-1} \\ \vdots & \ddots & \vdots \\ \tilde{x}_{N-1}^* & \dots & \tilde{x}_0 \end{pmatrix}, \tag{4.1.44}$$

where all entries are identically distributed. For that reason, $\tilde{\boldsymbol{x}}$ cannot be inverted explicitly analytically.

This is where chiral symmetry comes into play. We have learned in Section 3.4, that θ_0 determines if the system obeys average chiral symmetry. For $\theta_0 = 0 = \mu_0$, the staggered disorder potential that is represented by $\theta(x)$ is zero on average and therefore chiral symmetry on average remains, whereas a finite θ_0 (or μ_0) explicitly breaks the average chiral symmetry. We can directly translate these two cases to the structure of $\tilde{\boldsymbol{\mu}}$:

- For finite μ_0 with small fluctuations σ_μ on top, $\tilde{\boldsymbol{\mu}}$ is dominated by its diagonal. Hence, we can expand its inverse in powers of σ_μ. In this case, where we break chiral symmetry, we can therefore give an explicit expression for ϕ for sufficiently weak disorder.

- For average chiral symmetry $\mu_0 = 0$, this consideration does not work as $\tilde{\boldsymbol{\mu}}$ is completely random. In this case we have to rely on a numerical analysis.

We can determine the transition between these two regimes by the following consideration. The inverse

$$\tilde{\boldsymbol{\mu}}^{-1} = \frac{1}{\mu_0\sqrt{2N+1}} \frac{1}{\mathbb{1} + \frac{\sigma_\mu}{\mu_0}\frac{\tilde{\boldsymbol{x}}}{\sqrt{2N+1}}} \tag{4.1.45}$$

can be understood as the sum of the geometric series

$$\frac{1}{\mu_0\sqrt{2N+1}} \left(\mathbb{1} - \frac{\sigma_\mu}{\mu_0}\frac{\tilde{\boldsymbol{x}}}{\sqrt{2N+1}} + \dots \right) = \frac{1}{\mu_0\sqrt{2N+1}} \sum_{n=0}^{\infty} \left(-\frac{\sigma_\mu}{\mu_0}\frac{\tilde{\boldsymbol{x}}}{\sqrt{2N+1}} \right)^n, \tag{4.1.46}$$

which however only converges if

$$\left\| \frac{\sigma_\mu}{\mu_0}\frac{\tilde{\boldsymbol{x}}}{\sqrt{2N+1}} \right\| < \|\mathbb{1}\|. \tag{4.1.47}$$

Using the standard 2-norm

$$\|A\|_2 = \sqrt{\sum_{ij} |A_{ij}|^2}\,, \tag{4.1.48}$$

we can estimate

$$\|\tilde{\boldsymbol{x}}\|_2 = \sqrt{\sum_{k,l=0}^{N-1} |\tilde{x}_{l-k}|^2} = \sqrt{\frac{1}{\sigma_\mu^2(2N+1)} \sum_{k,l=0}^{N-1} \sum_{m,n=0}^{2N} \underbrace{\delta\mu_m \delta\mu_n}_{\substack{\sim\sigma_\mu^2\delta_{mn} \\ \text{(Eq. (4.1.38))}}} e^{2\pi i(l-k)(m-n)/(2N+1)}}$$

$$\sim N\,. \tag{4.1.49}$$

As $\|\mathbb{1}_N\|_2 = \sqrt{N}$, for large N we can therefore conclude that for $\sigma_\mu \lesssim \mu_0\sqrt{2}$ the geometric series Eq. (4.1.46) converges and for $\sigma_\mu \ll \mu_0$ we can approximate

$$\tilde{\boldsymbol{\mu}}^{-1} = \frac{1}{\mu_0\sqrt{2N+1}}\,\mathbb{1} - \frac{\sigma_\mu}{\mu_0^2}\,\frac{\tilde{\boldsymbol{x}}}{2N+1} + \mathcal{O}\left(\left(\frac{\sigma_\mu}{\mu_0}\right)^2\right)\,. \tag{4.1.50}$$

For $\sigma_\mu \gtrsim \mu_0\sqrt{2}$, in particular for $\mu_0 = 0$, this consideration is not valid as Eq. (4.1.46) is divergent. Consequently, we have to study ϕ for the limits $\sigma_\mu \ll \mu_0$ and $\mu_0 = 0$ separately.

4.1.4. Scattering phase for broken chiral symmetry

In the limit where $\sigma_\mu \ll \mu_0$, the above approximation Eq. (4.1.50) holds and with Eq. (4.1.34) we can write

$$\tilde{m} = \frac{1}{2N+1}\,\frac{\sigma_\mu^2}{\mu_0}\,\sum_{k=1}^{N} |\tilde{x}_k|^2 + \mathcal{O}\left(\left(\frac{\sigma_\mu}{\mu_0}\right)^3\right) \tag{4.1.51}$$

and with Eqs. (4.1.34), (4.1.22)

$$\tilde{m}_0 = 1 + i\mu_0 + i\frac{\sigma_\mu \tilde{x}_0}{\sqrt{2N+1}}\,. \tag{4.1.52}$$

We thus have $\frac{\tilde{m}}{\tilde{m}_0} \sim \mathcal{O}\left(\left(\frac{\sigma_\mu}{\mu_0}\right)^2\right)$, such that we can simplify S (Eq. (4.1.33)) by expanding it in powers of σ_μ/μ_0 to obtain

$$S = -1 + \frac{2}{\tilde{m}_0}\left(1 + i\frac{\tilde{m}}{\tilde{m}_0}\right) + \mathcal{O}\left(\left(\frac{\sigma_\mu}{\mu_0}\right)^3\right) . \tag{4.1.53}$$

We then get

$$\begin{aligned}\phi =& - i \log S \\ =& - i \log\left(-1 + \frac{2}{1+i\mu_0}\right) - \frac{2}{1+\mu_0^2}\frac{\sigma_\mu \tilde{x}_0}{\sqrt{2N+1}} \\ &+ \frac{2}{(1+\mu_0^2)^2}\frac{\sigma_\mu^2}{\mu_0}\frac{1}{2N+1}\left(\sum_{k=1}^{N}|\tilde{x}_k|^2\,(1+\mu_0^2) + \mu_0^2\,\tilde{x}_0^2\right) + \mathcal{O}\left(\left(\frac{\sigma_\mu}{\mu_0}\right)^3\right)\end{aligned} \tag{4.1.54}$$

and with Eqs. (4.1.39) and (4.1.41)

$$\begin{aligned}\phi = -\theta_0 - \frac{\sigma_\theta\,\tilde{x}_0}{\sqrt{2N+1}} + \frac{\sigma_\theta^2}{\sin(\theta_0)}\frac{1}{2N+1}\left(\sum_{k=1}^{N}|\tilde{x}_k|^2 + \tilde{x}_0^2\sin^2\left(\frac{\theta_0}{2}\right)\right) \\ + \mathcal{O}\left(\left(\frac{\sigma_\theta}{\theta_0}\right)^3\right) .\end{aligned} \tag{4.1.55}$$

As the $\tilde{x}_k$ are the coefficients of the unitary discrete Fourier transform of independent standard normally-distributed random variables $\delta\mu_m/\sigma_\mu$ (Eq. (4.1.42)), they are as well independent and standard normally-distributed, which can be written as

$$\langle \tilde{x}_k \rangle = 0\,, \quad \langle \tilde{x}_k^* \tilde{x}_l \rangle = \langle \tilde{x}_{-k}\tilde{x}_l \rangle = \delta_{kl}\,. \tag{4.1.56}$$

We can therefore average over all $\tilde{x}_k$ to compute mean value and standard deviation of ϕ. More details on this step are given in Appendix C.1. We obtain

$$\langle\phi\rangle = -\theta_0 + \frac{\sigma_\theta^2}{2\sin(\theta_0)} - \frac{a}{L}\cdot\frac{\sigma_\theta^2}{2\tan(\theta_0)} + \mathcal{O}\left(\left(\frac{\sigma_\theta}{\theta_0}\right)^3\right) , \tag{4.1.57}$$

$$\sigma(\phi) = \sqrt{\frac{a}{L}}\,\sigma_\theta + \mathcal{O}\left(\left(\frac{\sigma_\theta}{\theta_0}\right)^2\right) . \tag{4.1.58}$$

Hence, the mean value of the scattering phase is given by the mean value of the interpolation parameter θ_0 plus correction terms depending quadratically on the disorder strength σ_θ. These corrections are similar to a drift term in a random-walk motion, *i.e.*, introducing disorder shifts the mean value of ϕ by an amount that depends on the strength of the disorder and does not decay with L.

The standard deviation of ϕ is proportional to the disorder strength σ_θ, *i.e.*, stronger disorder increases the amount of fluctuations of the scattering phase. However, $\sigma(\phi)$ decays as $1/\sqrt{L}$ with the boundary length. Thus, we see a self-averaging behavior as mentioned in Section 3.6. For large system sizes the system averages itself and fluctuations on the scattering phase are suppressed. In the limit of $L \to \infty$ the scattering phase will be given by a precise value, such that scattering becomes completely specular. A graphene boundary that breaks average chiral symmetry therefore behaves like a mirror if the disorder is weak enough.

4.1.5. Scattering phase with chiral symmetry

For $\mu_0 = 0$, where the chiral symmetry is on average preserved, we have

$$\tilde{m}_0 = 1 + i\frac{\sigma_\mu \tilde{x}_0}{\sqrt{2N+1}}\,, \tag{4.1.59}$$

and as $\tilde{m}$ can be shown numerically to be approximately N-independent, for large N we can approximate $\tilde{m}_0 \approx 1$ and further simplify

$$\begin{aligned} S &= 1 + 2i\tilde{m} - \frac{2\tilde{m}^2}{1 - i\tilde{m}} + \mathcal{O}\left(\frac{\sigma_\mu}{\sqrt{2N+1}}\right) \\ &= \frac{1 + i\tilde{m}}{1 - i\tilde{m}} + \mathcal{O}\left(\frac{\sigma_\mu}{\sqrt{2N+1}}\right). \end{aligned} \tag{4.1.60}$$

We obtain

$$\phi = \arg(S) = \operatorname{atan2}\left(\mathfrak{Re}(S), \mathfrak{Im}(S)\right) = \operatorname{atan2}\left(1 - \tilde{m}^2, 2\tilde{m}\right)\,, \tag{4.1.61}$$

where the atan2-function is closely related to the arctangent but adjusted such that it properly gives the angle between its arguments,

$$\operatorname{atan2}(x,y) = \begin{cases} \arctan\left(\frac{y}{x}\right)\,, & x > 0\,, \\ \arctan\left(\frac{y}{x}\right) + \operatorname{sign}(y)\pi\,, & x < 0 \text{ and } y \neq 0\,, \\ \pi\,, & x < 0 \text{ and } y = 0\,, \\ \operatorname{sign}(y)\frac{\pi}{2}\,, & x = 0\,. \end{cases} \tag{4.1.62}$$

We are now interested in the distribution of

$$\tilde{m} = \frac{\tilde{\mu}_\downarrow^\dagger \tilde{\boldsymbol{\mu}}^{-1} \tilde{\mu}_\downarrow}{\sqrt{2N+1}} = \frac{\sigma_\mu}{\sqrt{2N+1}}\, \tilde{x}_\downarrow^\dagger \tilde{\boldsymbol{x}}^{-1} \tilde{x}_\downarrow \,, \tag{4.1.63}$$

with $\tilde{x}_\downarrow = \tilde{\mu}_\downarrow/\sigma_\mu$. As stated previously, we cannot find a general analytic expression, therefore we need to rely on numerical studies. The probability density of $\tilde{m}$ to take the value x that we find numerically is

$$f_{\tilde{m}}(x) = \frac{1}{\pi} \frac{\gamma}{x^2+\gamma^2} \,, \tag{4.1.64}$$

with $\gamma \approx 0.642\, \sigma_\mu = 0.321\, \sigma_\theta$. This is a so-called Cauchy distribution, which has the special and intriguing property that it does not possess any cumulants, as the corresponding integrals do not converge. In particular, its variance is infinite. This is quite plausible considering the fact that it only decays as $1/x^2$ for large x, which is the slowest decay that a probability distribution on the real axis can have to still be normalizable. Thus, the tails are an essential part of the Cauchy distribution and can not simply be neglected. Instead of the standard deviation, the relevant quantity that specifies the width of a Cauchy distribution is therefore the scale parameter γ.

Another remarkable observation is the fact that the value of γ/σ_θ we obtain numerically is not universal, but depends weakly on the original distribution of the disorder $\theta(x_m)$. If we choose these parameters to be not normally distributed but to follow any other distribution, $\tilde{m}$ is still Cauchy distributed, but the scale parameter γ will also depend on the higher cumulants of the chosen disorder distribution.

However, the scattering phase ϕ is of course restricted to the interval $[0, 2\pi)$ by the atan2-function (Eq. (4.1.61)) and therefore does possess a standard deviation. Since $f_{\tilde{m}}$ is even and ϕ is an odd function of $\tilde{m}$, we directly see that

$$\langle \phi \rangle = 0 \,. \tag{4.1.65}$$

Knowing the distribution of $\tilde{m}$, we can numerically evaluate the integral in $\langle \phi^2 \rangle$ to obtain

$$\sigma(\phi) \approx 1.33 \sqrt{\sigma_\theta} \,. \tag{4.1.66}$$

We notice that contrary to the case of broken chiral symmetry, the mean value of ϕ does not any more include a drift term induced by disorder but is precisely zero. Not surprisingly, the standard deviation of ϕ increases with σ_θ, *i.e.*, fluctuations on ϕ still increase with the strength of the disorder. However, the dependence on σ_θ does qualitatively change compared to the case of broken chiral symmetry

discussed previously, since it is not any more a proportionality but goes $\propto \sqrt{\sigma_\theta}$. Hence, for small $\sigma_\theta \ll 1$ fluctuations of the scattering phase increase much faster than when chiral symmetry is broken. Very surprising is the fact that $\sigma(\phi)$ does not at all depend on the boundary length L. We conclude that the system does not average itself for large L, and even in the limit $L \to \infty$ fluctuations of the scattering phase remain finite. This means that the mirror effect breaks down when chiral symmetry is on average preserved, and the boundary will never reflect specularly.

4.2. Tight-binding approach

We now turn to the tight-binding description. Contrary to the boundary condition that we used on the Dirac equation to introduce a disordered edge, a random onsite potential within the tight-binding model can in general mix the two valleys of the graphene band structure and will therefore allow for a more realistic description of scattering, including the computation of inter-valley scattering r^2.

We start from the model explained in Section 3.3.2 with a disorder potential on the outermost sites of the lattice as shown in Fig. 4.1. In Section 4.2.1, the Hamiltonian of the tight-binding system is explicitly shown and the scattering matrix is computed analytically for $E_F = 0$. We will see in Section 4.2.2 that we can distinguish the limits of broken and preserved chiral symmetry very analogously to Section 4.1.3. Eventually, we discuss scattering results in these two limits in Sections 4.2.3 and 4.2.4.

4.2.1. Hamiltonian and computation of the scattering matrix

Consider the tight-binding basis $\{|m, n, j\rangle\}$. The state $|m, n, j\rangle$ represents the atomic orbital (Wannier function) on the lattice site specified by the indices m, n, j, where m labels the y-coordinate of the blue rectangular superlattice shown in Fig. 4.1 from 1 to ∞ within the lead, being 0 on the boundary sites, n labels the corresponding x-coordinate from 0 to $N - 1 = (L - 1)/a$, and j determines the position within each cell of the superlattice in the order specified in Fig. 4.1. These atomic orbitals are assumed to form a complete basis of the lead Hilbert space within the tight-binding approximation. Therefore, we can write states on the lead as

$$|\psi_L\rangle = \sum_{m=1}^{\infty} \sum_{n=0}^{N-1} \sum_{j=1}^{4} \psi_L(m, n, j)|m, n, j\rangle \,, \tag{4.2.1}$$

where $\psi_L(m, n, j) = \langle m, n, j|\psi_L\rangle$ is the amplitude of the lead wavefunction on the lattice site (m, n, j). Correspondingly, the state on the boundary is given by the orbital states on the boundary sites as

$$|\psi_B\rangle = \sum_{n=0}^{N-1} \psi_B(n)|0, n, 4\rangle \tag{4.2.2}$$

with an amplitude $\psi_B(n) = \langle 0, n, 4|\psi_B\rangle$ on the n-th boundary site. We can then write the combined wavefunction $\psi = \psi_L + \psi_B$ in a vector representation within

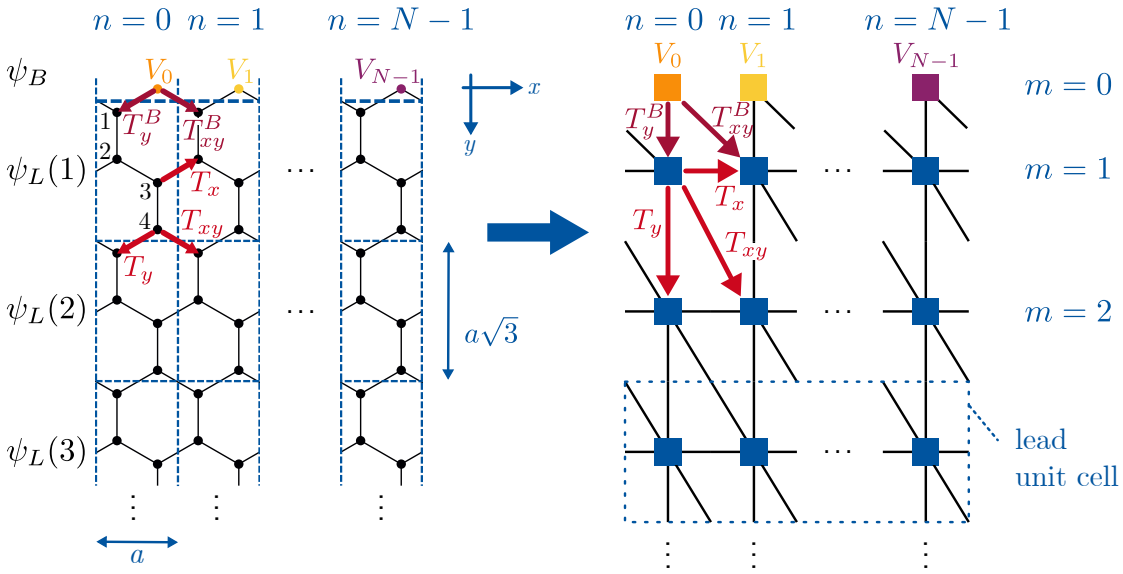

Figure 4.1.: Scheme of the tight-binding system for which the scattering matrix is computed, introducing a rectangular superlattice with four sites per unit cell. The superlattice unit cells are represented by blue squares in the right picture, defining a tight-binding system based on this superlattice. n labels the x-coordinate along the boundary from 0 to $N-1=(L-1)/a$ and m is the corresponding y-index going from 1 to ∞ as the lead has translational invariance in y-direction. The index $m=0$ indicates the boundary sites that do not belong to the lead. Numbers in the (1,1) unit cell (left) specify the order of the sites within each unit cell in the vector representation that will be used. As indicated by half lines, periodic boundary conditions are implemented by connecting the $n=N-1$ to the $n=0$ cells. V_n is the onsite disorder potential on the n-th boundary site and the T-s are the hopping matrices between adjacent superlattice unit cells within the lead and between lead and boundary (indicated by superscript B). ψ_B is the wavefunction amplitude on the boundary sites and $\psi_L(m)$ the one on the m-th unit cell of the lead (m-th row of the superlattice).

this basis by sorting the wavefunction amplitudes as

$$\psi=\begin{pmatrix}\psi_L\\ \psi_B\end{pmatrix}=\begin{pmatrix}\vdots\\ \psi_L(2)\\ \psi_L(1)\\ \psi_B\end{pmatrix}=\begin{pmatrix}\vdots\\ \psi_L(2,N-1)\\ \vdots\\ \psi_L(2,0)\\ \psi_L(1,N-1)\\ \vdots\\ \psi_L(1,0)\\ \psi_B(N-1)\\ \vdots\\ \psi_B(0)\end{pmatrix},\quad \psi_L(m,n)=\begin{pmatrix}\psi_L(m,n,1)\\ \psi_L(m,n,2)\\ \psi_L(m,n,3)\\ \psi_L(m,n,4)\end{pmatrix}. \tag{4.2.3}$$

The tight-binding Hamiltonian introduced in Eq. (2.2.2) in this basis reads

$$H = \sum_{mm'nn'jj'} t_{mnj,m'n'j'} |m,n,j\rangle\langle m',n',j'| = -t \sum_{\langle mnj,m'n'j'\rangle} |m,n,j\rangle\langle m',n',j'| \tag{4.2.4}$$

with the brackets under the second sum indicating that it goes only over nearest neighbors. We can write this in matrix form, using the same ordering as for ψ, as

$$H = \begin{pmatrix} \ddots & \ddots & & \\ \ddots & H_L & T_L & \\ & T_L^\dagger & H_L & T_{LB} \\ & & T_{LB}^\dagger & H_B \end{pmatrix} . \tag{4.2.5}$$

Here

$$H_L = \begin{pmatrix} H_0 & T_x & & T_x^\dagger \\ T_x^\dagger & H_0 & \ddots & \\ & \ddots & \ddots & T_x \\ T_x & & T_x^\dagger & H_0 \end{pmatrix} \tag{4.2.6}$$

is the $4N \times 4N$ Hamiltonian submatrix of each lead unit cell (row of the superlattice in Fig. 4.1, with fixed index $m \geq 1$),

$$H_B = \begin{pmatrix} V_{N-1} & & & \\ & \ddots & & \\ & & V_1 & \\ & & & V_0 \end{pmatrix} \tag{4.2.7}$$

is the $N \times N$ submatrix of the boundary (containing the onsite disorder potential on the diagonal), and

$$T_L = \begin{pmatrix} T_y & T_{xy} & & \\ & T_y & \ddots & \\ & & \ddots & T_{xy} \\ T_{xy} & & & T_y \end{pmatrix} , \qquad T_{LB} = \begin{pmatrix} T_y^B & T_{xy}^B & & \\ & T_y^B & \ddots & \\ & & \ddots & T_{xy}^B \\ T_{xy}^B & & & T_y^B \end{pmatrix} \tag{4.2.8}$$

couple consecutive lead unit cells and the $m = 1$ lead unit cell to the boundary, respectively. Their corresponding subblocks are given in terms of the hopping

parameter t by

$$H_0 = \begin{pmatrix} 0 & -t & 0 & 0 \\ -t & 0 & -t & 0 \\ 0 & -t & 0 & -t \\ 0 & 0 & -t & 0 \end{pmatrix}, \quad T_x = \begin{pmatrix} 0 & 0 & 0 & 0 \\ 0 & 0 & -t & 0 \\ 0 & 0 & 0 & 0 \\ 0 & 0 & 0 & 0 \end{pmatrix},$$
$$T_y = T_{xy} = \begin{pmatrix} 0 & 0 & 0 & -t \\ 0 & 0 & 0 & 0 \\ 0 & 0 & 0 & 0 \\ 0 & 0 & 0 & 0 \end{pmatrix}, \quad T_y^B = T_{xy}^B = \begin{pmatrix} -t \\ 0 \\ 0 \\ 0 \end{pmatrix}, \tag{4.2.9}$$

where H_0 contains all hoppings between sites within one superlattice unit cell and the T's the hoppings between adjacent cells, as sketched in Fig. 4.1. For simplicity and to keep expressions shorter, we will from now on set $t = 1$, *i.e.*, all energies such as the disorder potential will be given in units of t.

As outlined in Section 3.5, propagating and evanescent eigenmodes of the lead have to be computed to set up a system of equations that can be solved for the scattering matrix. The procedure to obtain the latter for a general tight-binding system is also explained in much detail in [15], which is therefore the starting point for the derivation of the scattering matrix. The calculation of S is somewhat lengthy but in principle analogous to the derivation of the scattering phase within the Dirac approximation presented in Section 4.1 and no new concepts are introduced. For this reason, the interested reader may refer to Appendix B to follow all steps in detail.

The scattering matrix that we obtain reads

$$S = \frac{1}{1 - \det Y + 2iY_{11}} \begin{pmatrix} 2\alpha Y_{12}^* & 1 + \det Y \\ 1 + \det Y & -2\alpha^* Y_{12} \end{pmatrix}, \tag{4.2.10}$$

where

$$\alpha = e^{i\pi/6}, \tag{4.2.11}$$

and the matrix Y is defined by Eq. (B.2.21) as

$$\begin{aligned} Y &= \begin{pmatrix} Y_{11} & Y_{12} \\ Y_{12}^* & Y_{11} \end{pmatrix} \\ &= \frac{1}{\sqrt{N}} \left[\begin{pmatrix} \tilde{V}_0 & \tilde{V}_{\frac{N}{3}} \\ \tilde{V}_{\frac{N}{3}}^* & \tilde{V}_0 \end{pmatrix} \right. \\ &\qquad \left. - \begin{pmatrix} \tilde{V}_1 & \dots & \tilde{V}_{\frac{N}{3}-1} \\ \tilde{V}_{\frac{N}{3}-1}^* & \dots & \tilde{V}_1^* \end{pmatrix} \begin{pmatrix} \tilde{V}_0 & \dots & \tilde{V}_{\frac{N}{3}-2} \\ \vdots & \ddots & \vdots \\ \tilde{V}_{\frac{N}{3}-2}^* & \dots & \tilde{V}_0 \end{pmatrix}^{-1} \begin{pmatrix} \tilde{V}_1^* & \tilde{V}_{\frac{N}{3}-1} \\ \vdots & \vdots \\ \tilde{V}_{\frac{N}{3}-1}^* & \tilde{V}_1 \end{pmatrix} \right] . \end{aligned} \tag{4.2.12}$$

It is derived in Appendix B.2 that due to periodic boundary conditions, N has to be a multiple of 3 to ensure that we have propagating modes at all. The Fourier coefficients of the disorder potential are defined by

$$\tilde{V}_k = \frac{1}{\sqrt{N}} \sum_{j=0}^{N-1} V_j \, e^{2\pi i (j-1)k/N} \, . \tag{4.2.13}$$

As stated in Section 3.5.1, the scattering matrix is essentially fixed by two relevant parameters, the inter-valley scattering probability r^2 and the intra-valley scattering phase ϕ, which can now be computed as

$$r^2 = |S_{11}|^2 = \frac{4|Y_{12}|^2}{(1 - \det Y)^2 + 4|Y_{11}|^2} \, , \tag{4.2.14}$$

$$\phi = \arg(S_{12}) = \operatorname{atan2}\big(1 - \det Y, -2Y_{11}\big) \, , \tag{4.2.15}$$

with the atan2-function defined in Eq. (4.1.62).

4.2.2. Implementation of chiral symmetry

We have thereby reduced the computation of the parameters r^2 and ϕ to a very similar problem as the one we faced in the Dirac approach in Section 4.1. Again, we have to invert a Hermitian Toeplitz matrix,

$$\tilde{\boldsymbol{V}} = \begin{pmatrix} \tilde{V}_0 & \dots & \tilde{V}_{\frac{N}{3}-2} \\ \vdots & \ddots & \vdots \\ \tilde{V}_{\frac{N}{3}-2}^* & \dots & \tilde{V}_0 \end{pmatrix} , \tag{4.2.16}$$

to obtain an explicit expression for S as a function of the disorder potential. It was discussed in Section 4.1.3 how we can distinguish two limits of this problem that refer to breaking and preserving chiral symmetry.

As the V_j are assumed to be normally distributed with mean value V_0 and standard deviation V, we can write them as

$$V_j = V_0 + V x_j \,, \tag{4.2.17}$$

such that the dimensionless quantities x_j are independent and standard normally distributed, *i.e.*, they have zero mean value and standard deviation equal to one, expressed by

$$\langle x_j \rangle = 0 \,, \quad \langle x_i x_j \rangle = \delta_{ij} \,. \tag{4.2.18}$$

With these definitions we can write the Fourier coefficients of the disorder potential (Eq. (4.2.13)) as

$$\tilde{V}_k = \frac{1}{\sqrt{N}} \sum_{j=0}^{N-1} (V_0 + V x_j)\, e^{2\pi i (j-1)k/N} = \sqrt{N} V_0 \, \delta_{k,0} + V \tilde{x}_k \,, \tag{4.2.19}$$

with

$$\tilde{x}_k = \frac{1}{\sqrt{N}} \sum_{j=0}^{N-1} x_j e^{2\pi i (j-1)k/N} \,. \tag{4.2.20}$$

Due to the unitarity of the Fourier transform, the complex Fourier coefficients $\tilde{x}_k$ are as well independent and standard normally distributed as expressed in Eq. (4.1.56). We use Eq. (4.2.19) to write $\tilde{\boldsymbol{V}}$ as

$$\tilde{\boldsymbol{V}} = \sqrt{N} V_0 \, \mathbb{1} + V \tilde{\boldsymbol{x}} \,, \quad \tilde{\boldsymbol{x}} = \begin{pmatrix} \tilde{x}_0 & \dots & \tilde{x}_{\frac{N}{3}-2} \\ \vdots & \ddots & \vdots \\ \tilde{x}^*_{\frac{N}{3}-2} & \dots & \tilde{x}_0 \end{pmatrix} \,. \tag{4.2.21}$$

This form is completely equivalent to the one of the matrix $\tilde{\boldsymbol{\mu}}$ within the Dirac approach, expressed by Eq. (4.1.43). Therefore, we can apply exactly the same reasoning as in Section 4.1.3. If $V \ll V_0$, *i.e.*, if we explicitly break the average chiral symmetry, we can approximate $\tilde{\boldsymbol{V}}^{-1}$ by a geometric series as

$$\tilde{\boldsymbol{V}}^{-1} = \frac{1}{\sqrt{N} V_0} \, \mathbb{1} - \frac{V}{V_0^2} \, \frac{\tilde{\boldsymbol{x}}}{N} + \mathcal{O}\left(\left(\frac{V}{V_0} \right)^2 \right) \,. \tag{4.2.22}$$

For $V \gtrsim V_0\sqrt{3}$, and in particular for $V_0 = 0$, this approximation breaks down and we have to invert the random Toeplitz matrix $\tilde{\boldsymbol{x}}$, which can only be done numerically. Therefore, in the next two subsections we will again study the parameters r^2 and ϕ for the limits $V \ll V_0$ (breaking chiral symmetry) and $V_0 = 0$ (preserving chiral symmetry) separately.

4.2.3. Scattering matrix for broken chiral symmetry

In the limit $V \ll V_0$ the approximation Eq. (4.2.22) will hold and with the definitions

$$\tilde{x}_\uparrow = \begin{pmatrix} \tilde{x}_{\frac{N}{3}-1} \\ \vdots \\ \tilde{x}_1 \end{pmatrix}, \quad \tilde{x}_\downarrow = \begin{pmatrix} \tilde{x}_1^* \\ \vdots \\ \tilde{x}_{\frac{N}{3}-1}^* \end{pmatrix}, \tag{4.2.23}$$

the coefficients of the matrix Y defined in Eq. (4.2.12) can be straightforwardly evaluated as

$$Y_{11} = V_0 + \frac{V}{\sqrt{N}}\tilde{x}_0 - \frac{V^2}{NV_0}\tilde{x}_\downarrow^\dagger \tilde{x}_\downarrow + \mathcal{O}\left(\left(\frac{V}{V_0}\right)^3\right), \tag{4.2.24}$$

$$Y_{12} = \frac{V}{\sqrt{N}}\tilde{x}_{\frac{N}{3}} - \frac{V^2}{NV_0}\tilde{x}_\downarrow^\dagger \tilde{x}_\uparrow + \mathcal{O}\left(\left(\frac{V}{V_0}\right)^3\right). \tag{4.2.25}$$

Inserting these expressions into the definitions of r^2 and ϕ (Eqs. (4.2.14), (4.2.15)) and keeping terms up to second order in V/V_0, we obtain

$$r^2 = \frac{4V^2}{N(1+V_0^2)^2}\,|\tilde{x}_{\frac{N}{3}}|^2 + \mathcal{O}\left(\left(\frac{V}{V_0}\right)^3\right), \tag{4.2.26}$$

$$\begin{aligned}\phi = & -\arctan\left(\frac{2V_0}{1-V_0^2}\right) - \frac{2V}{\sqrt{N}(1+V_0^2)}\,\tilde{x}_0 \\ & + \frac{2V^2}{NV_0(1+V_0^2)^2}\left(V_0^2\left(|\tilde{x}_0|^2 + |\tilde{x}_{\frac{N}{3}}|^2\right) + \left(1+V_0^2\right)\tilde{x}_\downarrow^\dagger \tilde{x}_\downarrow\right) \\ & + \mathcal{O}\left(\left(\frac{V}{V_0}\right)^3\right).\end{aligned} \tag{4.2.27}$$

With use of Eq. (4.1.56), we can then average over all disorder configurations as explained in Appendix C.1 to get

$$\langle r^2 \rangle = \frac{a}{L} \frac{4V^2}{(1+V_0^2)^2} + \mathcal{O}\left(\left(\frac{V}{V_0}\right)^3\right) , \tag{4.2.28}$$

$$\sigma(r^2) = \frac{a}{L} \frac{4V^2}{(1+V_0^2)^2} + \mathcal{O}\left(\left(\frac{V}{V_0}\right)^3\right) , \tag{4.2.29}$$

and

$$\begin{aligned} \langle \phi \rangle = & -\arctan\left(\frac{2V_0}{1-V_0^2}\right) \\ & + \frac{2}{3} \frac{V^2}{V_0\,(1+V_0^2)} - \frac{a}{L} \cdot \frac{2\,(1-V_0^2)}{V_0\,(1+V_0^2)^2}\, V^2 + \mathcal{O}\left(\left(\frac{V}{V_0}\right)^3\right) , \end{aligned} \tag{4.2.30}$$

$$\sigma(\phi) = 2\sqrt{\frac{a}{L}} \frac{V}{(1+V_0^2)} + \mathcal{O}\left(\left(\frac{V}{V_0}\right)^2\right) . \tag{4.2.31}$$

The mean value and the standard deviation of the inter-valley scattering probability r^2 show an identical behavior. Both increase quadratically with the disorder strength V, but are suppressed as $1/L$ with the boundary length L, thus clearly showing a self-averaging behavior. In the limit of $L \to \infty$, the system averages itself and inter-valley scattering vanishes. The mean of the intra-valley scattering phase ϕ changes from 0 to $-\pi/2$ when shifting the disorder mean from 0 to 1. In second order in V we have additional corrections that do not decay with L. This form of a constant and a drift-term is in perfect agreement to the results from the continuum description, presented in Eq. (4.1.57). Also fluctuations of the scattering phase show the same behavior as obtained from the Dirac equation (cf. Eq. (4.1.58)). The standard deviation of ϕ is proportional to the disorder strength but decays as $1/\sqrt{L}$, such that in the limit $L \to \infty$ the scattering phase is given by a precise value. In contrast to the result of the Dirac approach from Eq. (4.1.58), we however gain an additional dependence on the disorder mean V_0.

In Figs. 4.2 and 4.3 the analytical results for the mean and the standard deviation of r^2 and ϕ are compared to numerical simulations. Within the numerical approach, the same scattering problem is solved numerically for a fixed random distribution of the disorder potential. The mean and the standard deviation of r^2 and ϕ are computed by averaging over 10^3 configurations of the disorder potential for each value of V at fixed $V_0 = t$. For small $V \ll V_0$ we see a very good agreement between numerical and analytical results. Thus, we can conclude that the results presented in Eqs. (4.2.28)–(4.2.31) indeed correctly describe the low-V

regime. However, these approximations break down when the disorder strength V is of the order of the disorder mean V_0, as expected from the previous discussion in Section 4.2.2. For very strong disorder $V > V_0 = t$, scattering becomes independent of the boundary length. This means that the self-averaging ("mirror") effect breaks down, which is well consistent with our everyday experience, as a mirror becomes blurry when scratching it strongly enough. The mean value of r^2 in this large-V limit approaches $1/2$ and the standard deviation of ϕ gets large, *i.e.*, it becomes equally probable to scatter into any of the two valleys and the acquired phase gets completely random.

In summary, we find that if we break chiral symmetry by disorder with a finite mean value V_0, scattering shows self-averaging, as long as the disorder fluctuations are weak compared to the disorder mean, $V \ll V_0$. In the large-L limit we thereby regain purely specular reflection. The results for the scattering phase ϕ are in perfect agreement with the ones obtained from the Dirac equation, except for an additional weak dependence of the phase fluctuations on the disorder mean. Hence, for the kind of disorder we considered, neglecting inter-valley scattering is indeed a valid approximation to still describe the scattering phase correctly. For strong disorder $V \gtrsim V_0$ the self-averaging behavior breaks down and scattering becomes completely diffusive.

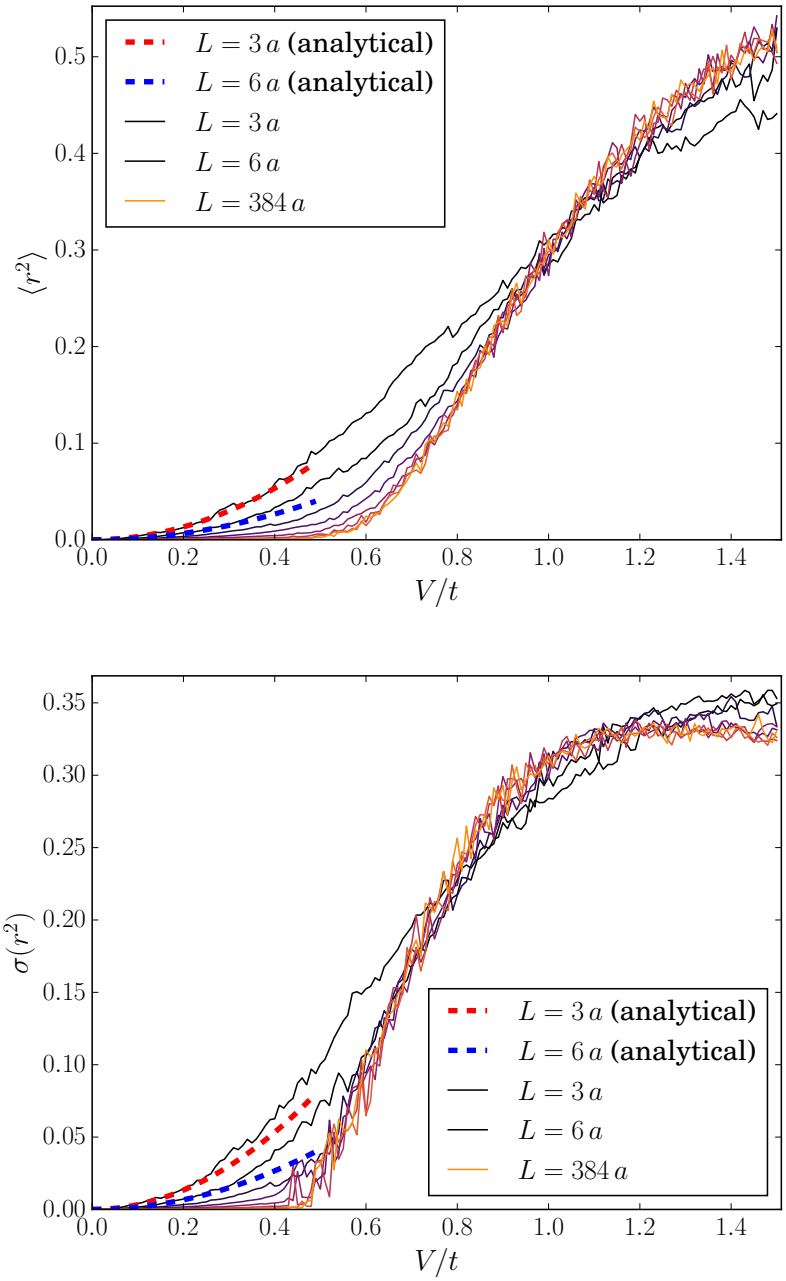

Figure 4.2.: Mean value $\langle r^2 \rangle$ and standard deviation $\sigma(r^2)$ of the inter-valley scattering probability as a function of the disorder strength V, computed within the tight-binding approximation for a disorder mean of $V_0 = t$. Numerical results are shown for logarithmically spaced boundary lengths ranging from $3a$ to $3 \cdot 2^7 a = 384a$, averaged over 10^3 disorder configurations. The analytical results in the low-V regime are plotted exemplarily for $L = 3a$ and $L = 6a$.

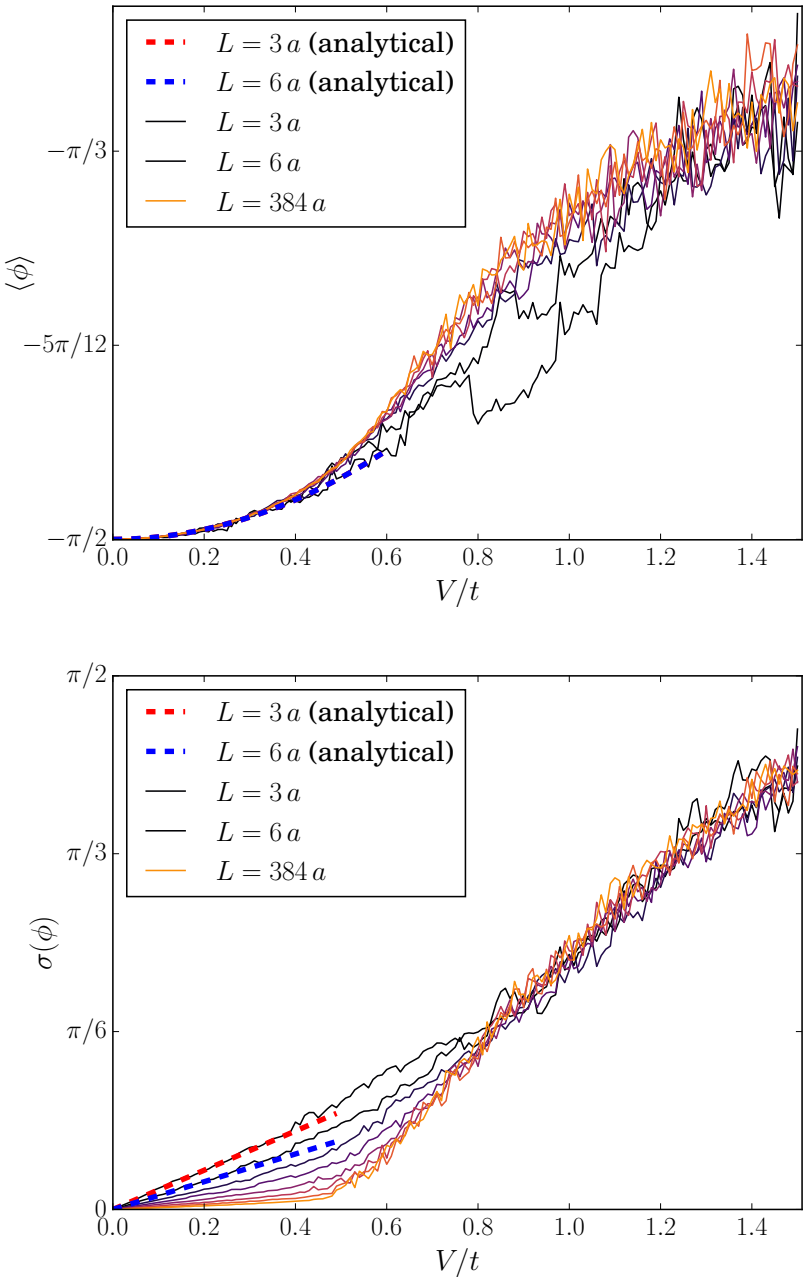

Figure 4.3.: Mean value $\langle\phi\rangle$ and standard deviation $\sigma(\phi)$ of the intra-valley scattering phase as a function of the disorder strength V, computed within the tight-binding approximation for a disorder mean of $V_0 = t$. Numerical results are shown for logarithmically spaced boundary lengths ranging from $3a$ to $3 \cdot 2^7 a = 384a$, averaged over 10^3 disorder configurations. The analytical results in the low-V regime are plotted exemplarily for $L = 3a$ and $L = 6a$.

4.2.4. Scattering matrix with chiral symmetry

As stated previously, for $V_0 = 0$ we cannot find an explicit expression for the scattering matrix parameters r^2 and ϕ depending on the boundary length $L = Na$. However, we can compute the corresponding expressions for each $N = 3, 6, \ldots$ individually. Averaging over the occuring Fourier coefficients of the disorder potential, we obtain for $N = 3$

$$\begin{aligned} \langle r_3^2 \rangle &= \tfrac{4}{3} V^2 + \mathcal{O}\left(V^3\right) , \qquad & \sigma(r_3^2) &= \tfrac{4}{3} V^2 + \mathcal{O}\left(V^3\right) , \\ \langle \phi_3 \rangle &= 0 , & \sigma(\phi_3) &= \sqrt{\tfrac{4}{3}} V + \mathcal{O}\left(V^2\right) , \end{aligned} \tag{4.2.32}$$

and for $N = 6$

$$\begin{aligned} \langle r_6^2 \rangle &= \sqrt{\tfrac{\pi}{3}} V + \mathcal{O}\left(V^2\right) , \qquad & \sigma(r_6^2) &= \sqrt[4]{\tfrac{\pi}{12}} \sqrt{V} + \mathcal{O}\left(V^{3/2}\right) , \\ \langle \phi_6 \rangle &= 0 , & \sigma(\phi_6) &= \sqrt{\sqrt{\tfrac{4\pi}{3}}\, \ln(2)}\, \sqrt{V} + \mathcal{O}\left(V\right) . \end{aligned} \tag{4.2.33}$$

Details on the calculation can be found in Appendix C.2.

For larger N, the expressions for r^2 and ϕ become very complicated rational functions and the multidimensional integrals that occur in the disorder averages are unfeasible to be evaluated analytically. More refined numerical calculations within the low-V regime, averaging over 10^6 disorder configurations, suggest that the prefactors change very weakly with N, but it is not clear if they will converge for $N \to \infty$. Furthermore, we know from the results of the Dirac approach in Section 4.1.5 that the exact prefactors are not universal but additionally depend on the distribution of the disorder potential. Therefore, we would not gain new insights by computing the exact analytical expressions for larger N. Instead, we rely on numerical computations and compare them to the analytical solutions for $N = 3$ and $N = 6$ for a qualitative discussion, as the latter very well resembles the behavior for any $N \geq 6$ qualitatively.

The numerical results and the analytical expressions of Eqs. (4.2.32) and (4.2.33) are shown in Figs. 4.4 and 4.5. We see a big qualitative difference between the cases of $N = 3$ and $N \geq 6$. This is most likely due to the structure of the evanescent modes. For $N = 3$ the system is so small that only a single evanescent mode exists, whereas for $N \geq 6$ a new class of evanescent modes (χ_ν^+, see Appendix B.2) is available. Since a sample with a boundary length of 3 unit cells ($< 1\,\mathrm{nm}$) is anyway far from being a realistic setup, we will not bother further about this case.

For $N \geq 6$ both parameters r^2 and ϕ are mainly independent of N, such that in agreement with the results from the Dirac approach no self-averaging happens and the boundary does not behave like a mirror. The inter-valley scattering probability increases linearly with the disorder strength for small $V \ll 1$ and its standard

deviation even as $\sqrt{V}$, contrary to the quadratic dependence we have seen for broken chiral symmetry $V_0 > 0$. Therefore, inter-valley scattering dramatically increases for small V, compared to the case of broken chiral symmetry $V_0 \neq 0$. The same is true for fluctuations of the scattering phase ϕ. The results of ϕ are very much in accordance with the ones from the continuum model. The mean value of ϕ is exactly zero, meaning that the drift-term occurring in the case of broken chiral symmetry vanishes. Fluctuations of the scattering phase increase as $\sqrt{V}$ instead of a linear increase for weak disorder and are again not suppressed with increasing L.

Interestingly, the mean value of r^2 reaches about $2/3$ for strong disorder $V > 1$, indicating that in this limit it becomes more favorable to scatter into the opposite valley than staying in the same cone. However, we cannot find any plausible explanation for this observation. The standard deviation of the scattering phase $\sigma(\phi)$ becomes again large in this limit, such that ϕ becomes completely random.

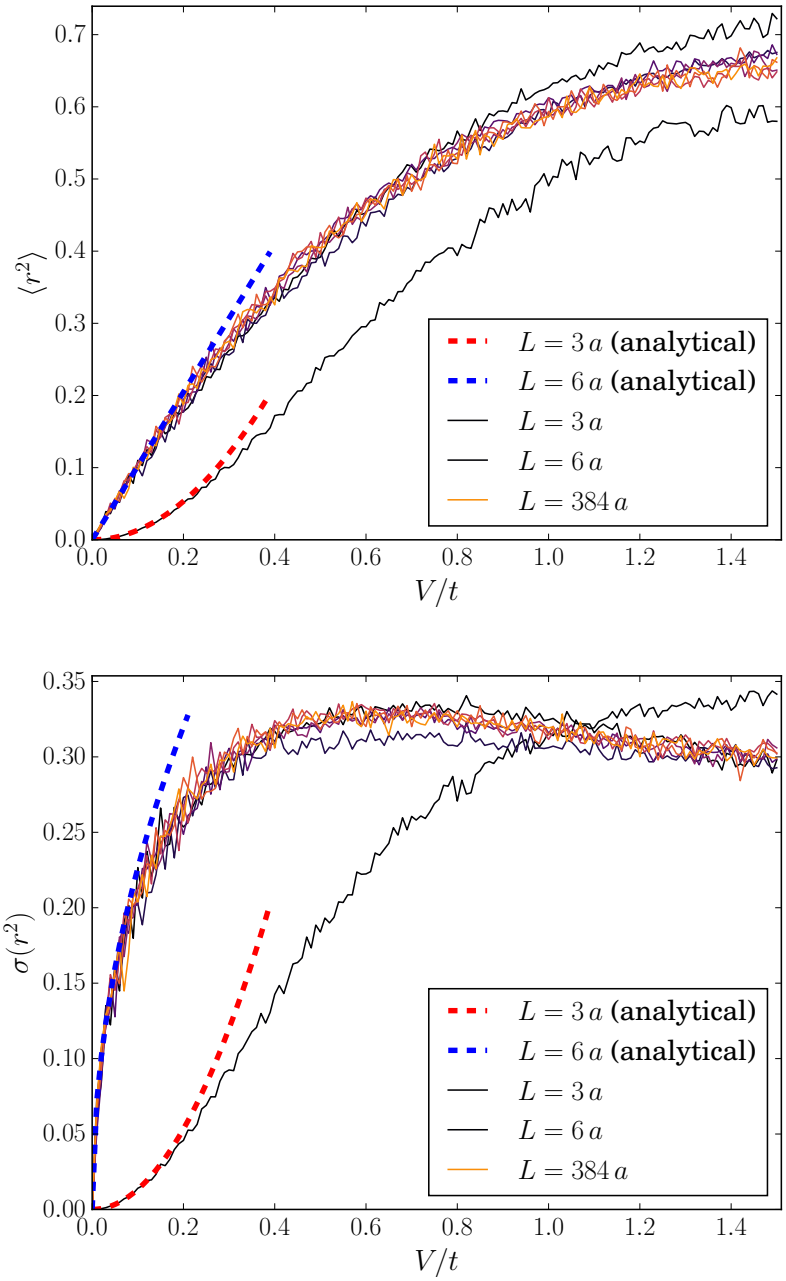

Figure 4.4.: Mean value $\langle r^2 \rangle$ and standard deviation $\sigma(r^2)$ of the inter-valley scattering probability as a function of the disorder strength V, computed within the tight-binding approximation for a disorder mean of $V_0 = 0$. Numerical results are shown for logarithmically spaced boundary lengths ranging from $3a$ to $3 \cdot 2^7 a = 384a$, averaged over 10^3 disorder configurations. The analytical results in the low-V regime are plotted exemplarily for $L = 3a$ and $L = 6a$.

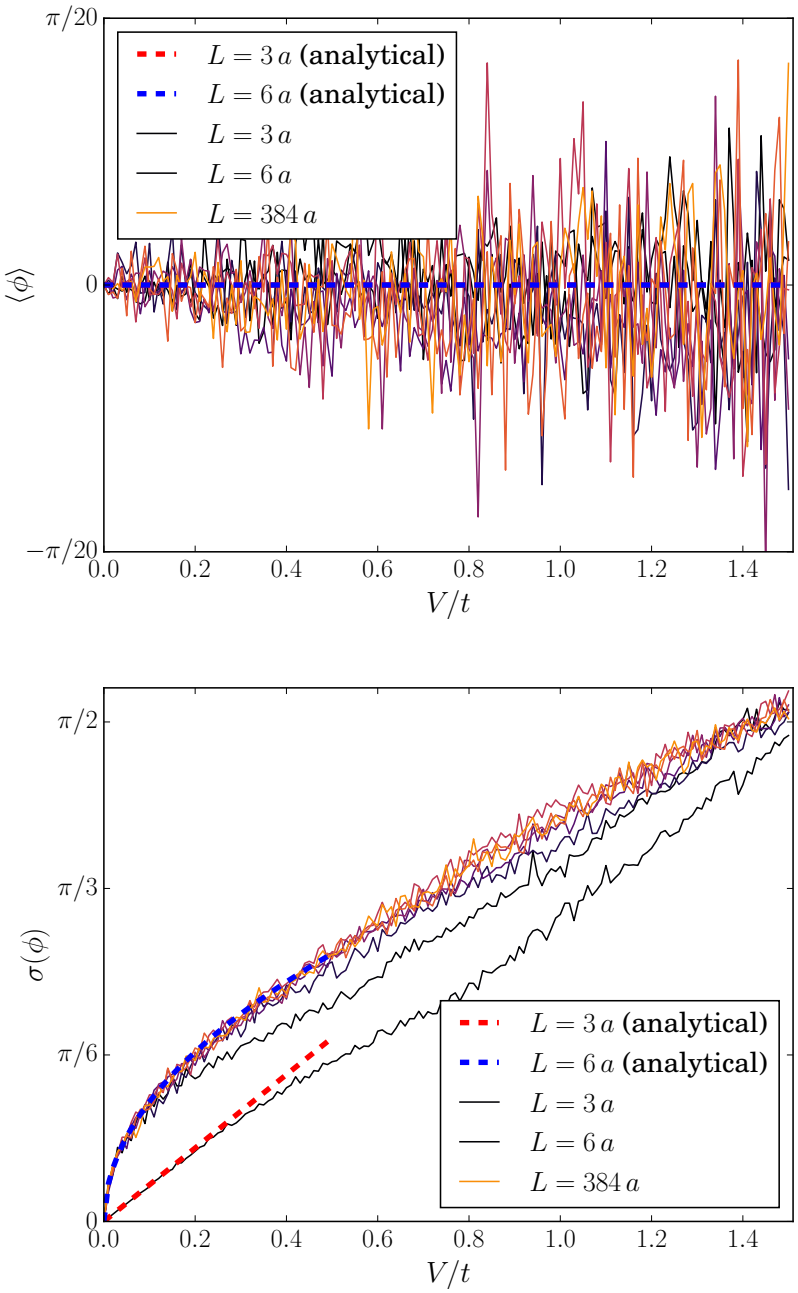

Figure 4.5.: Mean value $\langle\phi\rangle$ and standard deviation $\sigma(\phi)$ of the intra-valley scattering phase as a function of the disorder strength V, computed within the tight-binding approximation for a disorder mean of $V_0 = 0$. Numerical results are shown for logarithmically spaced boundary lengths ranging from $3a$ to $3 \cdot 2^7 a = 384a$, averaged over 10^3 disorder configurations. The analytical results in the low-V regime are plotted exemplarily for $L = 3a$ and $L = 6a$.

5. Scattering at finite doping

Finally, we study how the results obtained in the last chapter transfer to the more general case of finite dopings $E_F > 0$, where a potentially large number of modes can contribute to electronic transport. To this end, we solve the scattering problem within the tight-binding approximation from the model introduced in Section 3.3.2 at energies between $0.05t$ and $0.2t$, which are still small enough to be well in the linear regime of the graphene dispersion (Eq. (2.2.7)). The scattering matrix is computed numerically using the Python package *Kwant* [14], which is specifically designed for quantum transport calculations. The procedure of solving the scattering problem follows the general idea described in Section 3.5 and also explained in much detail in [15], and it is also analogous to the tight-binding computation at $E_F = 0$ shown in Appendix B (except for the much larger number of modes, which would make an analytic computation extremely cumbersome). For this reason, we will not discuss further details of the derivation of the scattering matrix here.

In Section 5.1 we shortly sketch the structure of the propagating modes in k-space at $E_F > 0$, and explain how we can describe diffusive scattering in terms of these modes. In Section 5.2 we then discuss the resulting diffusive scattering probability, depending on if chiral symmetry is broken or preserved.

5.1. Structure of the modes

For finite but small Fermi energy $E_F \ll t$, the Fermi surface can be mapped onto two approximately circular curves around the two Dirac points $\boldsymbol{K}$ and $\boldsymbol{K'}$ (Fig. 5.1). Due to periodic boundary conditions, the momentum in x-direction along the boundary is restricted (cf. Eq. (B.1.3)) by the condition

$$k_x L = 2\pi\nu\,, \quad \nu \in \mathbb{Z}\,. \tag{5.1}$$

Hence, propagating modes at a certain Fermi energy $E_F > 0$ correspond to points in k-space which are equally spaced along k_x and lie on the approximately circular Fermi surfaces, as depicted in Fig. 5.1. The velocity of the modes is given by

$$\boldsymbol{v} = \frac{1}{\hbar}\frac{\mathrm{d}E}{\mathrm{d}\boldsymbol{k}}\,, \tag{5.2}$$

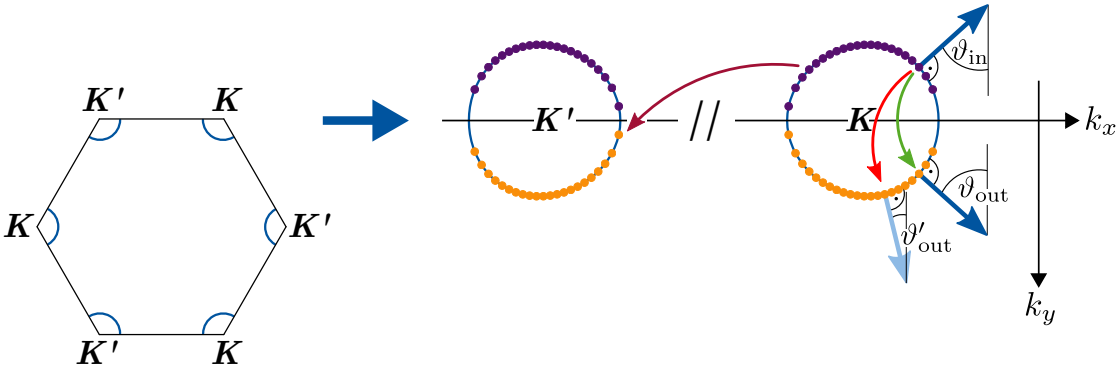

Figure 5.1.: Left: Fermi surface (blue) for $E_F = 0.1t$ within the first Brillouin zone (not to scale). Right: By shifting by reciprocal lattice vectors, the Fermi surface can be mapped onto two approximately circular shapes (distance of the two Dirac cones not to scale). Due to periodic boundary conditions, modes are equally spaced along k_x. Incoming modes are depicted by violet dots, outgoing modes by orange ones. Blue arrows indicate the direction of the velocity of the modes, which defines angles with respect to the boundary normal $\hat{\boldsymbol{y}}$. Specular reflection processes (green) do not change this angle, whereas diffusive ones (red) do. Also inter-valley processes with high momentum transfer (dark red) are diffusive.

thus it is normal to the Fermi surface. We can separate incoming and outgoing modes by their velocity in y direction. Incoming modes have a negative v_y (moving towards the boundary, violet in Fig. 5.1), outgoing ones have a positive v_y (orange in Fig. 5.1). With use of the velocity, we can easily assign to each mode an angle of incidence with respect to the boundary normal $\hat{\boldsymbol{y}}$, as defined in Fig. 5.1. As also described in Section 3.1, an incoming mode with the angle ϑ_{in} is reflected specularly, if the outgoing mode has an angle of $\vartheta_{\text{out}} = -\vartheta_{\text{in}}$. This is equivalent to saying that the momentum along the boundary k_x is conserved during the scattering process, and only the momentum k_y perpendicular to the boundary changes. One such specular reflection process is symbolized by a green arrow in Fig. 5.1. On the other hand side, during scattering processes which do not conserve momentum along the boundary, also the angle of the direction of propagation of the mode with respect to the boundary is changed from ϑ_{in} to $\vartheta'_{\text{out}} \neq -\vartheta_{\text{in}}$. Such processes we call diffusive, exemplarily shown by a red arrow in Fig. 5.1. Diffusive processes can happen within one cone, but also inter-valley scattering processes change the momentum strongly and therefore contribute to diffusive scattering (dark red arrow in Fig. 5.1). To study the influence of diffusive scattering in

general in a system with many modes, we consider the total diffusive scattering probability

$$P_{\text{diff}} = \frac{1}{N_M} \sum_{\substack{m,n \\ \psi_n^{\text{in}} \to \psi_m^{\text{out}} \\ \text{diffusive}}} |S_{mn}|^2 , \tag{5.3}$$

i.e., the sum of probabilities of all diffusive scattering processes from all incoming modes ψ_n^{in} to all outgoing modes ψ_m^{out}. Thereby, we average diffusive contributions over all N_M incoming modes.

5.2. Diffusive scattering with and without chiral symmetry

In Fig. 5.2, numerical results of P_{diff} are shown for Fermi energies between $0.05t$ and $0.2t$ as a function of the standard deviation V of the boundary onsite potential, which we have identified to express the strength of the disorder. The corresponding Fermi wavelengths range from $\approx 109a$ to $\approx 27a$ (Eq. (2.2.9)), and the boundary length is chosen as $L = 120a$ to always fulfill $L > \lambda_F$. We chose a mean value of the disorder potential of $V_0 = E_F$ and $V_0 = E_F - 0.2t$. Additionally, we averaged over 10^3 configurations of the disorder potential.

We see a huge qualitative difference between the two choices of the disorder mean V_0. For $V_0 \neq E_F$, the diffusive scattering probability increases quadratically for small V and is suppressed with increasing Fermi wavelength λ_F for small $V \ll (E_F - V_0)$. Hence, we observe a clear mirror effect, similar to the behavior of the inter-valley scattering probability for broken chiral symmetry observed at $E_F = 0$ (cf. Eq. (4.2.28) and Fig. 4.2). However, for $V_0 = E_F$ the increase of P_{diff} with V is linear and essentially independent of λ_F, just as the behavior of r^2 for preserved chiral symmetry at $E_F = 0$, shown in Fig. 4.4. We can conclude that for finite E_F and $V_0 = E_F$, chiral symmetry is on average preserved, leading to a qualitativ change in the scattering behavior and to a breakdown of the mirror effect. Moreover, the diffusive scattering increases for small V ($< 0.1t$) by two orders of magnitude compared to the case of $V_0 \neq E_F$, where chiral symmetry is explicitly broken.

This result, that chiral symmetry is on average preserved for $V_0 = E_F$, is consistent with the case $E_F = 0$ and also with the following consideration (cf. Fig. 5.3). If the mean value of the onsite potential is larger than zero on the boundary, the Dirac cones are shifted with respect to the bulk. Thereby, an onsite potential V_0 effectively shifts the chemical potential on the boundary locally by $-V_0$, as also discussed in Section 3.3.2. If $V_0 = E_F$, the chemical potential on the boundary

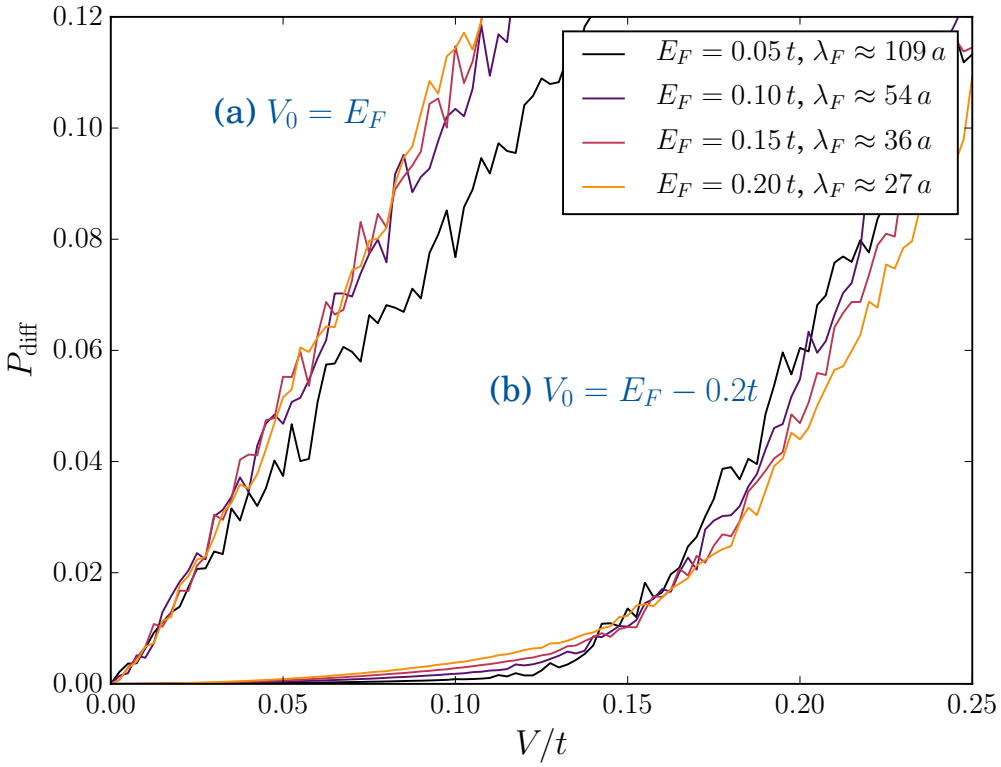

Figure 5.2.: Total diffusive scattering probability P_{diff}, averaged over all incoming modes, as a function of the disorder strength V. Numerical results are computed within the tight-binding approximation with use of *Kwant* [14], for a boundary length of $120a$ and averaged over 10^3 disorder configurations. The scattering problem is solved at Fermi energies ranging from $E_F = 0.05t$ to $E_F = 0.2t$, corresponding to Fermi wavelengths between $\approx 109a$ and $\approx 27a$. The disorder mean is chosen separately for each Fermi energy as $V_0 = E_F$ (a) and $V_0 = E_F - 0.2t$ (b).

is on average shifted down to the Dirac points, and chiral symmetry is on the boundary on average preserved, just as for $E_F = 0$ and $V_0 = 0$.

In summary, we find that the behavior observed for $E_F = 0$ equivalently occurs for finite E_F. For a disorder potential with a mean value $V_0 \neq E_F$ which breaks chiral symmetry, the diffusive scattering probability is suppressed with increasing Fermi wavelength λ_F. Hence, the system averages itself and in the large Fermi wavelength limit the boundary reflects specularly like a mirror. On the other hand side, a disorder mean of $V_0 = E_F$ leads to a breakdown of this mirror effect

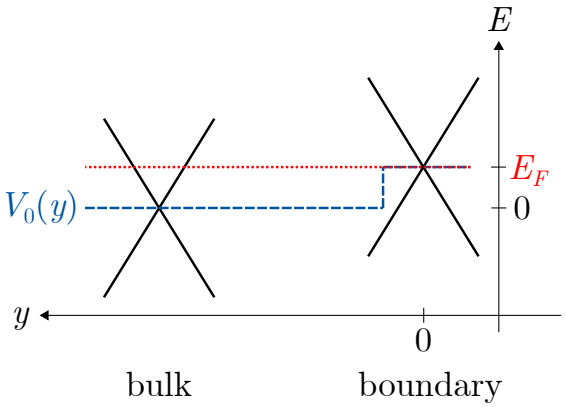

Figure 5.3.: Schematic sketch of the linear part of the graphene dispersion (Dirac cone) at different positions y on the graphene sheet (for simplicity only one cone is shown). A finite mean value $V_0 > 0$ of the onsite potential on the boundary shifts the Dirac cone up with respect to the bulk, thereby effectively shifting down the chemical potential. An onsite potential of $V_0 = E_F$ shifts the chemical potential on the boundary to the Dirac point.

and hence to a strong increase of diffusive scattering.

6. Conclusion

In this thesis, we studied scattering at a single disordered graphene boundary within the scattering matrix formalism. We explained that we can model disorder within the continuum model of the Dirac equation by using appropriate position-dependent boundary conditions on the Dirac spinor wavefunctions, and within the tight-binding approximation by introducing a random onsite potential. Further, we showed that we can analytically solve for the scattering matrix in both approaches, assuming the Fermi energy to be directly at the Dirac points. Within the continuum model, the chosen boundary conditions do not mix the two valleys of the graphene dispersion, hence we studied only a single valley. In this case we remain with one incoming and one outgoing propagating mode. We computed the distribution of the scattering phase that is acquired during the scattering process, providing information about the "diffusiveness" of scattering. In the tight-binding approach, we additionally allowed for inter-valley scattering, therefore computing the intra-valley scattering phase and the inter-valley scattering probability. The results of both approaches agree very well.

If the disorder breaks chiral symmetry, we can compute explicit analytical expressions for the scattering matrix for weak enough disorder. We find a quadratic increase of the inter-valley scattering probability r^2 and a linear increase of fluctuations of the intra-valley scattering phase ϕ with the disorder strength V, and a random-walk-like drift term for the mean value of the scattering phase that is quadratic in V. More importantly, we find that inter-valley scattering as well as fluctuations on the scattering phase are suppressed with the boundary length L as $1/L$, clearly indicating a self-averaging behavior. For large boundary lengths, diffusive scattering vanishes and the boundary reflects specularly, hence behaving similar to a classical mirror. Only in the regime of very strong disorder V, we find numerically that it becomes equally probable to scatter into any of the two cones, and fluctuations on the scattering phase become large. In this limit scattering on the boundary is thus completely diffusive.

On the other hand side, if the disorder is chosen such that it preserves chiral symmetry on average, the situation is very different. Both mean value and fluctuations of the inter-valley scattering probability r^2 as well as fluctuations of the scattering phase ϕ qualitatively change their behavior for weak disorder, showing a significant increase compared to the case of broken chiral symmetry. Very unexpectedly, the scattering phase even follows a Cauchy distribution. Additionally,

all those parameters do not any more decay with the boundary length. Therefore, we observe a breakdown of the expected mirror effect, as even for large boundary lengths diffusive scattering remains finite and the boundary never reflects specularly.

Numerical studies at finite doping show a very similar behavior. In accordance with the analytically studied case of scattering at the Dirac points and with intuitive expectations, the preservation of chiral symmetry occurs if the disorder mean matches the Fermi energy, $V_0 = E_F$. In this case we see again a breakdown of the mirror effect and a significant increase of the diffusive scattering probability, compared to the case of a mismatch $V_0 \neq E_F$ where chiral symmetry is broken and the mirror works, *i.e.*, diffusive scattering becomes small for large Fermi wavelengths.

The very unexpected effect observed in this thesis, that chiral symmetry can lead to a breakdown of a mirror-like behavior of a disordered graphene boundary, should in principle also be observable in experiment. This could be achieved by tuning the disorder mean on the boundary with a gate and focusing incoming electrons onto the boundary, *e.g.*, with a magnetic field. When the disorder potential is tuned such that chiral symmetry is on average conserved, the boundary should not any more behave like a mirror and diffusive scattering should increase strongly, which one would then be able to observe as a decrease of the device conductance.

A. Parametrization of the scattering matrix at the Dirac points

At the Dirac points, the scattering matrix is of size 2×2. We can find a useful parametrization as follows. We start from a general complex matrix

$$S = \begin{pmatrix} r_1 e^{i\varphi_1} & r_3 e^{i\varphi_3} \\ r_3 e^{i\varphi_3} & r_2 e^{i\varphi_2} \end{pmatrix} \tag{A.1}$$

that we choose to be symmetric due to time-reversal symmetry (Eq. (3.5.12)). From the unitarity condition Eq. (3.5.11) we obtain

$$r_1 = r_2 = r \quad \text{and} \quad r_3 = \sqrt{1 - r^2}\,, \tag{A.2}$$

and additionally

$$e^{i(\varphi_1 - \varphi_3)} + e^{i(\varphi_3 - \varphi_2)} = 0\,. \tag{A.3}$$

Defining

$$\varphi_1 = \phi + \Delta_1\,, \tag{A.4}$$
$$\varphi_2 = \phi + \Delta_2\,, \tag{A.5}$$
$$\varphi_3 = \phi\,, \tag{A.6}$$

we obtain

$$e^{i\Delta_1} = -e^{-i\Delta_2} \tag{A.7}$$

and thereby with $\Delta_1 = \Delta$

$$S = e^{i\phi} \begin{pmatrix} r e^{i\Delta} & \sqrt{1 - r^2} \\ \sqrt{1 - r^2} & -r e^{-i\Delta} \end{pmatrix}\,. \tag{A.8}$$

B. Scattering matrix in the tight-binding approach

B.1. Lead eigenstates

Consider the tight-binding Hamiltonian defined in Eq. (4.2.5) in Section 4.2.1. As explained in Section 3.5, we will in a first step ignore the boundary and assume the lead to have translational invariance also in negative y-direction. This can be easily accomplished by writing the Hamiltonian and the lead wavefunction as

$$H_L^{\text{inf}} = \begin{pmatrix} \ddots & \ddots & & \\ \ddots & H_L & T_L & \\ & T_L^\dagger & H_L & \ddots \\ & & \ddots & \ddots \end{pmatrix}, \quad \psi_L^{\text{inf}} = \begin{pmatrix} \vdots \\ \psi_L(2) \\ \psi_L(1) \\ \vdots \end{pmatrix}. \tag{B.1.1}$$

As we know that this infinite lead has translational invariance in x- and in y-direction, we use a Bloch ansatz for the lead wavefunction, writing

$$\psi_L^{\text{inf}}(m,n) = \lambda^m \xi^n \chi\,, \tag{B.1.2}$$

where λ and ξ are eigenvalues of the translation operator in y- and x-direction, respectively. The 4-vector χ gives the mode structure within each superlattice unit cell. Note that this Bloch ansatz lives on the rectangular superlattice. We thereby disregard the original honeycomb lattice structure and assume the hoppings T_x and T_y to be exactly aligned with the x- and y-axis, respectively, as shown in Fig. 4.1 on the right. This means that we choose the mode structure χ within a unit cell to be multiplied by a factor of ξ when hopping along T_x, by λ when hopping along T_y, and by $\xi\lambda$ for hoppings T_{xy}. This choice amounts to a specific gauge of the phase of the wavefunction. Hence, it is completely equivalent to choosing Bloch phases according to the honeycomb structure by, *e.g.*, assuming also a phase shift in y-direction for hoppings T_x.

As we have periodic boundary conditions $\psi_L^{\text{inf}}(m,n) = \psi_L^{\text{inf}}(m,n+N)$, it must

hold that $\xi^N = 1$, therefore we have

$$\xi_\nu = e^{ik_{x,\nu}a} = e^{2\pi i\nu/N} \quad \text{with} \quad k_{x,\nu} = \frac{2\pi\nu}{L} = \frac{2\pi}{a}\frac{\nu}{N}\,, \quad \nu = 0, \ldots, N-1\,. \tag{B.1.3}$$

At $E_F = 0$, the Fermi surface consists only of the Dirac points, so propagating modes have a momentum that lies at these points in momentum space. Therefore, the momentum $k_{x,\nu}$ must match the x-component of the Dirac points for some ν to have propagating modes at all, such that we demand $k_{x,\nu} = K_x = 2\pi/3a$ or $k_{x,\nu} = K'_x = -2\pi/3a$ (Eq. (2.1.4)). We conclude that $N \overset{!}{=} 3\nu$, thus propagating modes are only possible if the boundary length L is a multiple of $3a$, which we in the following will assume to be true.

Using the Bloch ansatz, the Schrödinger equation for the infinite lead at $E_F = 0$ reduces to

$$H_L^{\text{inf}}\psi_L^{\text{inf}} = 0 \quad \overset{\text{Eq. (B.1.2)}}{\Rightarrow} \quad H_c\chi = 0\,, \tag{B.1.4}$$

with

$$H_c = H_0 + \left(\xi_\nu^{-1}T_x + \lambda^{-1}T_y + \xi_\nu^{-1}\lambda^{-1}T_{xy} + \text{h.c.}\right)\,. \tag{B.1.5}$$

Hence, we reduced the infinite-dimensional eigenvalue problem of Eq. (B.1.1) to one of dimension 4×4, from which we can get the mode structure χ within each lead unit cell. By solving $\det H_c = 0$, we obtain the relations

$$\lambda_\nu^+ = \frac{(1+\xi_\nu)^2}{\xi_\nu}\,, \quad \lambda_\nu^- = \frac{\xi_\nu}{(1+\xi_\nu)^2} \tag{B.1.6}$$

between the translation operator eigenvalues ξ and λ that need to be fulfilled for H_c to have a zero eigenvalue. Thereby for each possible x-momentum $k_{x,\nu}$ we have two solutions for the momentum in y-direction defined through

$$\lambda_\nu = e^{ik_{y,\nu}a}\,. \tag{B.1.7}$$

As we in fact restrict the lattice to positive y, modes do not have to be normalizable for negative y. Therefore, we can allow for all λ with $|\lambda| \leq 1$, *i.e.*, for plane waves and modes that decay exponentially for $y \to \infty$, as also stated in Section 3.5. This also means that the momentum k_y does not have to be real but can also have a positive imaginary part.

We get the corresponding eigenmodes as

$$\chi_\nu^+ = \begin{pmatrix} 0 \\ -1 \\ 0 \\ 1+\xi_\nu \end{pmatrix}, \quad \chi_\nu^- = \begin{pmatrix} -1-\xi_\nu \\ 0 \\ \xi_\nu \\ 0 \end{pmatrix}. \tag{B.1.8}$$

Regarding their translation eigenvalue $\lambda_\nu^\pm$, these lead eigenmodes can be classified as follows:

Propagating modes: Modes with $\xi_{\boldsymbol{K}} = \xi_{N/3} = e^{2\pi i/3}$ and $\xi_{\boldsymbol{K'}} = \xi_{2N/3} = e^{-2\pi i/3}$ have $\lambda = 1$ and thus are propagating (their amplitudes do not decay in y-direction). Defining

$$\Phi_{\mathrm{pr}} = (\chi_{\boldsymbol{K}}^-, \chi_{\boldsymbol{K}}^+, \chi_{\boldsymbol{K'}}^-, \chi_{\boldsymbol{K'}}^+), \quad \Xi_{\mathrm{pr}} = \mathrm{diag}(\xi_{\boldsymbol{K}}, \xi_{\boldsymbol{K}}, \xi_{\boldsymbol{K'}}, \xi_{\boldsymbol{K'}}), \quad \Lambda_{\mathrm{pr}} = \mathbb{1}_4, \tag{B.1.9}$$

the set of propagating modes on the m-th lead unit cell is given by

$$\Psi_{\mathrm{pr}}\Lambda_{\mathrm{pr}}^m = \begin{pmatrix} \Phi_{\mathrm{pr}}\,\Xi_{\mathrm{pr}}^{N-1} \\ \vdots \\ \Phi_{\mathrm{pr}}\,\Xi_{\mathrm{pr}} \\ \Phi_{\mathrm{pr}} \end{pmatrix} \Lambda_{\mathrm{pr}}^m. \tag{B.1.10}$$

To separate incoming and outgoing states, we have to find eigenstates of the particle current operator [15]

$$J = \frac{2a}{\hbar}\mathfrak{Im}(\Lambda_{\mathrm{pr}}^* T_L) \tag{B.1.11}$$

within the set of propagating modes. Therefore we have to diagonalize

$$J_{\mathrm{pr}} = \Psi_{\mathrm{pr}}^\dagger J \Psi_{\mathrm{pr}} = \frac{2a}{\hbar}\,\Psi_{\mathrm{pr}}^\dagger\,\mathfrak{Im}(\Lambda_{\mathrm{pr}}^* T_L)\,\Psi_{\mathrm{pr}} = \frac{a}{i\hbar}\,\Psi_{\mathrm{pr}}^\dagger (T_L - T_L^\dagger)\Psi_{\mathrm{pr}}. \tag{B.1.12}$$

J_{pr} can be straightforwardly evaluated from the definitions above, with Eq. (2.2.8) yielding

$$J = \frac{4}{\sqrt{3}}\,N v_F \begin{pmatrix} 0 & -\alpha & & \\ -\alpha^* & 0 & & \\ & & 0 & \alpha^* \\ & & \alpha & 0 \end{pmatrix}, \tag{B.1.13}$$

where

$$\alpha = \xi_{\boldsymbol{K}}^{1/4} = e^{i\pi/6}\,. \tag{B.1.14}$$

The eigenvalues of J are $-\frac{4}{\sqrt{3}}\,Nv_F$ (corresponding to incoming modes moving in negative y-direction, towards the boundary) with normalized eigenvectors $v_{\boldsymbol{K}}^- = \frac{1}{\sqrt{2}}(\alpha, 1, 0, 0)^T$ and $v_{\boldsymbol{K'}}^- = \frac{1}{\sqrt{2}}(0, 0, -\alpha^*, 1)^T$, and $+\frac{4}{\sqrt{3}}\,Nv_F$ (corresponding to outgoing modes) with eigenvectors $v_{\boldsymbol{K}}^+ = \frac{1}{\sqrt{2}}(-\alpha, 1, 0, 0)^T$ and $v_{\boldsymbol{K'}}^+ = \frac{1}{\sqrt{2}}(0, 0, \alpha^*, 1)^T$. Since we sorted the propagating modes by the two valleys (Eq. (B.1.9)) and these eigenvectors do not mix the subspaces of the two valleys, we can also assign each to a unique valley by labeling them $\boldsymbol{K}, \boldsymbol{K'}$.

To ensure that S is unitary, all propagating lead eigenmodes have to be properly normalized to carry the same probability current. However, as here all modes have already the same current eigenvalue according to its absolute value, we can choose any normalization that simplifies the calculation. With

$$\Phi_{\text{in}} = \Phi_{\text{pr}} \cdot (v_{\boldsymbol{K}}^-,\, v_{\boldsymbol{K'}}^-)/\sqrt{N}\,, \quad \Xi_{\text{in}} = \text{diag}(\xi_{\boldsymbol{K}},\, \xi_{\boldsymbol{K'}})\,, \quad \Lambda_{\text{in}} = \mathbb{1}_2\,, \quad \text{and} \tag{B.1.15}$$

$$\Phi_{\text{out}} = \Phi_{\text{pr}} \cdot (v_{\boldsymbol{K'}}^+,\, v_{\boldsymbol{K}}^+)/\sqrt{N}\,, \quad \Xi_{\text{out}} = \text{diag}(\xi_{\boldsymbol{K'}},\, \xi_{\boldsymbol{K}})\,, \quad \Lambda_{\text{out}} = \mathbb{1}_2\,, \tag{B.1.16}$$

we can therefore define incoming and outgoing modes with current normalized to $\mp 4v_F/\sqrt{3}$ and well-defined momenta $k_x = 2\pi/3, k_x = -2\pi/3$ on the m-th lead unit cell within the notation introduced in Eq. (4.2.3) as

$$(\psi_{\boldsymbol{K}}^{\text{in}}(m), \psi_{\boldsymbol{K'}}^{\text{in}}(m)) = \Psi_{\text{in}}\Lambda_{\text{in}}^m = \begin{pmatrix} \Phi_{\text{in}}\,\Xi_{\text{in}}^{N-1} \\ \vdots \\ \Phi_{\text{in}}\,\Xi_{\text{in}} \\ \Phi_{\text{in}} \end{pmatrix} \Lambda_{\text{in}}^m\,, \tag{B.1.17}$$

$$(\psi_{\boldsymbol{K'}}^{\text{out}}(m), \psi_{\boldsymbol{K}}^{\text{out}}(m)) = \Psi_{\text{out}}\Lambda_{\text{out}}^m = \begin{pmatrix} \Phi_{\text{out}}\,\Xi_{\text{out}}^{N-1} \\ \vdots \\ \Phi_{\text{out}}\,\Xi_{\text{out}} \\ \Phi_{\text{out}} \end{pmatrix} \Lambda_{\text{out}}^m\,. \tag{B.1.18}$$

Note that we sort the outgoing modes in opposite order with respect to the valleys as the incoming modes. This is to ensure that they reflect time-reversal symmetry (cf. Eq. (3.5.5)). Under time-reversal the velocity of the modes is reversed and the valleys are exchanged. Therefore, with this ordering the outgoing modes are the time-reversed incoming ones.

Evanescent modes: For $-N/3 < \nu < N/3$ holds $\lambda_\nu^- < 1$ and $\lambda_\nu^+ > 1$, thus χ_ν^--modes are evanescent (they decay for $y \to \infty$, starting from a finite value at the boundary), whereas χ^+-modes are not normalizable. For $N/3 < \nu < 2N/3 = -N/3 \mod N$ the opposite case is true. The normalization of the evanescent modes is irrelevant for the result of the calculation of S, therefore we multiply them with $1/\sqrt{N}$ which will later simplify prefactors. We can then simply write the set of evanescent modes within the m-th lead unit cell as

$$\left(\psi^{\mathrm{ev}}_{-\frac{N}{3}+1}(m), \ldots, \psi^{\mathrm{ev}}_{\frac{N}{3}-1}(m), \psi^{\mathrm{ev}}_{\frac{N}{3}+1}(m), \ldots, \psi^{\mathrm{ev}}_{\frac{2N}{3}-1}(m)\right) = \Psi_{\mathrm{ev}}\Lambda_{\mathrm{ev}} = (\Psi^-_{\mathrm{ev}}\Lambda^-_{\mathrm{ev}}, \Psi^+_{\mathrm{ev}}\Lambda^+_{\mathrm{ev}})\,, \tag{B.1.19}$$

where

$$\Psi^\mp_{\mathrm{ev}} = \frac{1}{\sqrt{N}} \begin{pmatrix} \Phi^\mp_{\mathrm{ev}} & (\Xi^\mp_{\mathrm{ev}})^{N-1} \\ & \vdots \\ \Phi^\mp_{\mathrm{ev}} & \Xi^\mp_{\mathrm{ev}} \\ & \Phi^\mp_{\mathrm{ev}} \end{pmatrix}, \quad \Lambda_{\mathrm{ev}} = \mathrm{diag}(\Lambda^-_{\mathrm{ev}}, \Lambda^+_{\mathrm{ev}})\,, \tag{B.1.20}$$

with

$$\Phi^-_{\mathrm{ev}} = (\chi^-_{-\frac{N}{3}+1}, \ldots, \chi^-_{\frac{N}{3}-1})\,, \tag{B.1.21}$$

$$\Xi^-_{\mathrm{ev}} = \mathrm{diag}(\xi_{-\frac{N}{3}+1}, \ldots, \xi_{\frac{N}{3}-1})\,, \tag{B.1.22}$$

$$\Lambda^-_{\mathrm{ev}} = \mathrm{diag}(\lambda^-_{-\frac{N}{3}+1}, \ldots, \lambda^-_{\frac{N}{3}-1})\,, \tag{B.1.23}$$

and

$$\Phi^+_{\mathrm{ev}} = (\chi^+_{\frac{N}{3}+1}, \ldots, \chi^+_{\frac{2N}{3}-1})\,, \tag{B.1.24}$$

$$\Xi^+_{\mathrm{ev}} = \mathrm{diag}(\xi_{\frac{N}{3}+1}, \ldots, \xi_{\frac{2N}{3}-1})\,, \tag{B.1.25}$$

$$\Lambda^+_{\mathrm{ev}} = \mathrm{diag}(\lambda^+_{\frac{N}{3}+1}, \ldots, \lambda^+_{\frac{2N}{3}-1})\,. \tag{B.1.26}$$

B.2. Computation of the scattering matrix

In a second step we want to set up a system of equations for the scattering matrix of the boundary as described in Section 3.5. To achieve this, we can use the eigenstates of the infinite lead to compose scattering states in the leads, now assuming to have the boundary terminating the lead, which are given in the m-th

lead unit cell by

$$\Psi_L(m) = (\psi_{\boldsymbol{K}}(m), \psi_{\boldsymbol{K'}}(m)) = \Psi_{\text{in}}\Lambda_{\text{in}}^m + \Psi_{\text{out}}\Lambda_{\text{out}}^m S + \Psi_{\text{ev}}\Lambda_{\text{ev}}^m S_{\text{ev}}\,, \tag{B.2.1}$$

Each of these two scattering states is a superposition of a fixed incoming mode with momentum $\boldsymbol{K}$ or $\boldsymbol{K'}$, outgoing modes into which the incoming mode has been reflected at the boundary (expressed by the scattering matrix S), and evanescent modes, where S_{ev} gives the amplitudes to scatter into them, equivalently to S.

With $\Psi_B = (\psi_{B,\boldsymbol{K}}, \psi_{B,\boldsymbol{K'}})$, where the additional subscript $\boldsymbol{K}, \boldsymbol{K'}$ distinguishes the boundary wavefunctions depending on the momentum of the incoming modes, the last two blocks of the Schrödinger equation

$$H \begin{pmatrix} \Psi_L \\ \Psi_B \end{pmatrix} = 0 \tag{B.2.2}$$

yield

$$\begin{pmatrix} T_L\Psi_{\text{out}} & T_L\Psi_{\text{ev}} & -T_{LB} \\ T_{LB}^\dagger\Psi_{\text{out}}\Lambda_{\text{out}} & T_{LB}^\dagger\Psi_{\text{ev}}\Lambda_{\text{ev}} & H_B \end{pmatrix} \begin{pmatrix} S \\ S_{\text{ev}} \\ \Psi_B \end{pmatrix} = \begin{pmatrix} -T_L\Psi_{\text{in}} \\ -T_{LB}^\dagger\Psi_{\text{in}}\Lambda_{\text{in}} \end{pmatrix}. \tag{B.2.3}$$

This is a linear system of $4N$ equations with $4N$ unknowns, which are the components of the scattering matrix S, those of the scattering matrix of the evanescent modes S_{ev}, and the boundary wavefunction Ψ_B. The matrix on the left that defines the system contains the disorder potentials V_j on the boundary sites via H_B. Therefore, by solving this system of equations for the scattering matrix, we can obtain S as a function of all V_j as discussed in Section 3.5. In principle we can easily solve the system numerically for any N by inverting the matrix on the left. However, we are interested in an analytic solution as a function of N to study the dependence of the relevant parameters of S on the boundary length $L = Na$. Solving the above system of equations for S analytically requires more effort than a numerical matrix inversion, but in principle the procedure is also somehow straightforward.

First, we realize that $T_L\Psi_{\text{ev}}^- = 0$, $T_{LB}^\dagger\Psi_{\text{ev}}^+ = 0$, such that we can simplify further to

$$\begin{pmatrix} T_L\Psi_{\text{out}} & 0 & T_L\Psi_{\text{ev}}^+ & -T_{LB} \\ T_{LB}^\dagger\Psi_{\text{out}}\Lambda_{\text{out}} & T_{LB}^\dagger\Psi_{\text{ev}}^-\Lambda_{\text{ev}}^- & 0 & H_B \end{pmatrix} \begin{pmatrix} S \\ S_{\text{ev}}^- \\ S_{\text{ev}}^+ \\ \Psi_B \end{pmatrix} = \begin{pmatrix} -T_L\Psi_{\text{in}} \\ -T_{LB}^\dagger\Psi_{\text{in}}\Lambda_{\text{in}} \end{pmatrix}. \tag{B.2.4}$$

Due to the banded structure of T_L and T_{LS} it seems to be useful to apply a discrete

Fourier transform of both equation blocks by multiplying from the left by

$$\begin{pmatrix} U \otimes \mathbb{1}_4 & 0 \\ 0 & U \end{pmatrix}, \quad U_{mn} = \frac{1}{\sqrt{N}} e^{2\pi i (N-m)(N-n)/N} = \frac{1}{\sqrt{N}} e^{2\pi i mn/N}. \tag{B.2.5}$$

We obtain

$$\begin{pmatrix} (U \otimes \mathbb{1}_4) T_L \Psi_{\text{out}} & 0 & (U \otimes \mathbb{1}_4) T_L \Psi_{\text{ev}}^{+} & -(U \otimes \mathbb{1}_4) T_{LB} U^\dagger \\ U T_{LB}^\dagger \Psi_{\text{out}} \Lambda_{\text{out}} & U T_{LB}^\dagger \Psi_{\text{ev}}^{-} \Lambda_{\text{ev}}^{-} & 0 & U H_B U^\dagger \end{pmatrix} \begin{pmatrix} S \\ S_{\text{ev}}^{-} \\ S_{\text{ev}}^{+} \\ U \Psi_B \end{pmatrix} = \begin{pmatrix} -(U \otimes \mathbb{1}_4) T_L \Psi_{\text{in}} \\ -U T_{LB}^\dagger \Psi_{\text{in}} \Lambda_{\text{in}} \end{pmatrix}. \tag{B.2.6}$$

By explicitly computing all blocks of the system using the definitions given before, we get

$$\left(\begin{array}{cccc|c} 0 & 0 & 0 & 0 & \\ -A_2 & 0 & 0 & 0 & \\ 0 & 0 & 0 & \Lambda_{\text{ev}}^{+} & \mathbb{1} + \Xi^\dagger \\ -A_1 & 0 & 0 & 0 & \\ 0 & 0 & 0 & 0 & \\ \hline 0 & 0 & \Xi_{\text{ev}}^{->} & 0 & \\ \alpha^* A_2 & 0 & 0 & 0 & \\ 0 & 0 & 0 & 0 & U H_B U^\dagger \\ -\alpha A_1 & 0 & 0 & 0 & \\ 0 & \Xi_{\text{ev}}^{-<} & 0 & 0 & \end{array}\right) \begin{pmatrix} S \\ S_{\text{ev}}^{-<} \\ S_{\text{ev}}^{->} \\ S_{\text{ev}}^{+} \\ U \Psi_B \end{pmatrix} = \left(\begin{array}{c} 0 \\ A_1 \\ 0 \\ A_2 \\ 0 \\ \hline 0 \\ \alpha^* A_1 \\ 0 \\ -\alpha A_2 \\ 0 \end{array}\right) \tag{B.2.7}$$

with

$$A_1 = \left(\frac{1}{\sqrt{2}}, 0\right), \quad A_2 = \left(0, \frac{1}{\sqrt{2}}\right), \tag{B.2.8}$$

and

$$\Xi_{\mathrm{ev}}^{-<} = \mathrm{diag}(\xi_{-\frac{N}{3}+1}, \ldots, \xi_0)\,, \tag{B.2.9}$$

$$\Xi_{\mathrm{ev}}^{->} = \mathrm{diag}(\xi_1, \ldots, \xi_{\frac{N}{3}-1})\,, \tag{B.2.10}$$

$$\Xi_{\mathrm{ev}}^{-} = \mathrm{diag}(\Xi_{\mathrm{ev}}^{-<}, \Xi_{\mathrm{ev}}^{->})\,, \tag{B.2.11}$$

and

$$\Xi = \mathrm{diag}(\xi_1, \ldots, \xi_N) = \mathrm{diag}(\Xi_{\mathrm{ev}}^{->}, \xi_{\boldsymbol{K}}, \Xi_{\mathrm{ev}}^{+}, \xi_{\boldsymbol{K'}}, \Xi_{\mathrm{ev}}^{-<})\,. \tag{B.2.12}$$

Correspondingly, the evanescent modes scattering matrix S_{ev} is split up into parts for the same momentum ranges as

$$S_{\mathrm{ev}} = \begin{pmatrix} S_{\mathrm{ev}}^{-<} \\ S_{\mathrm{ev}}^{->} \\ S_{\mathrm{ev}}^{+} \end{pmatrix} \tag{B.2.13}$$

The lower right block of Eq. (B.2.7) has the form

$$UH_BU^\dagger = \frac{1}{\sqrt{N}} \begin{pmatrix} \tilde{V}_0 & \tilde{V}_1 & \ldots & \tilde{V}_{N-1} \\ \tilde{V}_1^* & \tilde{V}_0 & \ddots & \vdots \\ \vdots & \ddots & \ddots & \tilde{V}_1 \\ \tilde{V}_{N-1}^* & \ldots & \tilde{V}_1^* & \tilde{V}_0 \end{pmatrix}\,, \tag{B.2.14}$$

with the Fourier coefficients of the disorder potential

$$\tilde{V}_k = \frac{1}{\sqrt{N}} \sum_{j=0}^{N-1} V_j\, e^{2\pi i(j-1)k/N}\,. \tag{B.2.15}$$

By clever pivoting, *i.e.*, exchanging the rows and columns of Eq. (B.2.7), we can bring the system into a block-diagonal form where the lower right $((N/3+3) \times (N/3+3))$-block does not depend on S_{ev}, thus leaving us with

$$\begin{pmatrix} \bar{V} & B_1 \\ C & D_1 \end{pmatrix} \begin{pmatrix} \bar{\Psi} \\ S \end{pmatrix} = \begin{pmatrix} B_2 \\ D_2 \end{pmatrix}\,. \tag{B.2.16}$$

Here $\bar{\Psi}$ contains some of the components of $U\Psi_B$ which however will be eliminated in the procedure of solving for S and therefore do not need to be specified. The

matrix

$$\bar{V} = \frac{1}{\sqrt{N}} \left(\begin{array}{ccc|cc} \tilde{V}_0 & \dots & \tilde{V}_{\frac{N}{3}-2} & \tilde{V}_1^* & \tilde{V}_{\frac{N}{3}-1} \\ \vdots & \ddots & \vdots & \vdots & \vdots \\ \tilde{V}_{\frac{N}{3}-2}^* & \dots & \tilde{V}_0 & \tilde{V}_{\frac{N}{3}-1}^* & \tilde{V}_1 \\ \hline \tilde{V}_1 & \dots & \tilde{V}_{\frac{N}{3}-1} & \tilde{V}_0 & \tilde{V}_{\frac{N}{3}} \\ \tilde{V}_{\frac{N}{3}-1}^* & \dots & \tilde{V}_1^* & \tilde{V}_{\frac{N}{3}}^* & \tilde{V}_0 \end{array} \right) \tag{B.2.17}$$

contains only the lowest third of the Fourier components of the disorder potential V_j. Further, the remaining blocks of the system are given by

$$\begin{aligned} C &= \left(\begin{array}{ccc|cc} 0 & \dots & 0 & 1+\xi_{\boldsymbol{K'}} & 0 \\ 0 & \dots & 0 & 0 & 1+\xi_{\boldsymbol{K}} \end{array} \right), \\ B_1 &= \left(\begin{array}{cc} 0 & 0 \\ \vdots & \vdots \\ 0 & 0 \\ \hline 0 & \frac{\alpha^*}{\sqrt{2}} \\ \frac{-\alpha}{\sqrt{2}} & 0 \end{array} \right), \quad B_2 = \left(\begin{array}{cc} 0 & 0 \\ \vdots & \vdots \\ 0 & 0 \\ \hline \frac{\alpha^*}{\sqrt{2}} & 0 \\ 0 & \frac{-\alpha}{\sqrt{2}} \end{array} \right), \\ D_1 &= \begin{pmatrix} 0 & -\frac{1}{\sqrt{2}} \\ -\frac{1}{\sqrt{2}} & 0 \end{pmatrix}, \quad D_2 = \begin{pmatrix} \frac{1}{\sqrt{2}} & 0 \\ 0 & \frac{1}{\sqrt{2}} \end{pmatrix}. \end{aligned} \tag{B.2.18}$$

Assuming the invertibility of $\bar{V}$ and $D_1 - C\bar{V}^{-1}B_1$, we can use the block matrix inversion formula (Eq. (4.1.27)) to solve Eq. (B.2.16) by multiplying with $\begin{pmatrix} \bar{V} & B_1 \\ C & D_1 \end{pmatrix}^{-1}$ from the left. We thereby obtain

$$S = \left[D_1 - C\bar{V}^{-1}B_1 \right]^{-1} \left(D_2 - C\bar{V}^{-1}B_2 \right), \tag{B.2.19}$$

reducing the problem to the inversion of $\bar{V}$. Due to the structure of B_1, B_2, and

C, we only need to know the lower right 2×2 block of $\bar{V}^{-1}$, which we denote by

$$\bar{V}^{-1} = \left(\begin{array}{ccc|cc} \ddots & & & \ddots & \\ & \ddots & & & \ddots \\ \hline \ddots & & & W_{11} & W_{12} \\ & \ddots & & W_{21} & W_{22} \end{array}\right) . \tag{B.2.20}$$

As $\bar{V}$ (and therefore also W) is Hermitian, it must hold that $W_{11}, W_{22} \in \mathbb{R}$ and $W_{21} = W_{12}^*$. Further, from the structure of $\bar{V}$ we conclude that $W_{11} = W_{22}$. We formally obtain $Y = W^{-1}$ by again using block-matrix inversion. Due to Eq. (4.1.27), Y is given by the Schur complement of the upper left block of $\bar{V}$ as

$$\begin{aligned} Y &= \begin{pmatrix} Y_{11} & Y_{12} \\ Y_{12}^* & Y_{11} \end{pmatrix} \\ &= \frac{1}{\sqrt{N}} \left[\begin{pmatrix} \tilde{V}_0 & \tilde{V}_{\frac{N}{3}} \\ \tilde{V}_{\frac{N}{3}}^* & \tilde{V}_0 \end{pmatrix} \right. \\ &\qquad \left. - \begin{pmatrix} \tilde{V}_1 & \dots & \tilde{V}_{\frac{N}{3}-1} \\ \tilde{V}_{\frac{N}{3}-1}^* & \dots & \tilde{V}_1^* \end{pmatrix} \begin{pmatrix} \tilde{V}_0 & \dots & \tilde{V}_{\frac{N}{3}-2} \\ \vdots & \ddots & \vdots \\ \tilde{V}_{\frac{N}{3}-2}^* & \dots & \tilde{V}_0 \end{pmatrix}^{-1} \begin{pmatrix} \tilde{V}_1^* & \tilde{V}_{\frac{N}{3}-1} \\ \vdots & \vdots \\ \tilde{V}_{\frac{N}{3}-1}^* & \tilde{V}_1 \end{pmatrix} \right] . \end{aligned} \tag{B.2.21}$$

From Eq. (B.2.19) we can straightforwardly write down S in terms of the Y_{ij}, resulting in Eq. (4.2.10).

C. Computation of disorder averages

C.1. Disorder averages and Wick's theorem

In the process of computing any parameter X of the scattering matrix as a function of the mean value and the standard deviation of the disorder, in both the Dirac and the tight-binding approach we need to compute expressions like

$$\langle X(x_0,\ldots,x_{N-1})\rangle = \int_{-\infty}^{\infty} \mathrm{d}x_0 f(x_0)\cdots\int_{-\infty}^{\infty} \mathrm{d}x_{N-1} f(x_{N-1})\; X(x_0,\ldots,x_{N-1})\,, \tag{C.1.1}$$

or similarly in terms of the Fourier coefficients of the disorder as

$$\langle X(\tilde{x}_0,\ldots\tilde{x}_{N-1})\rangle = \int \mathrm{d}\tilde{x}_0 \tilde{f}(\tilde{x}_0)\cdots\int \mathrm{d}\tilde{x}_{N-1} \tilde{f}(\tilde{x}_{N-1})\; X(\tilde{x}_0,\ldots\tilde{x}_{N-1})\,. \tag{C.1.2}$$

Here $f(x_j)$ or $\tilde{f}(\tilde{x}_k)$ are the probability distributions of the disorder parameter x_j or $\tilde{x}_k$, respectively, which are each normalized to have unit standard deviation. (In the Dirac approach we have to replace $N \to 2N+1$.) Since we expand r^2 and ϕ to second order in the $\tilde{x}_k$, knowing their distribution and correlations

$$\langle \tilde{x}_k\rangle = 0\,, \quad \langle \tilde{x}_k^* \tilde{x}_l\rangle = \langle \tilde{x}_{-k}\tilde{x}_l\rangle = \delta_{kl}\,, \tag{C.1.3}$$

(cf. Eq. (4.1.56)), we can easily evaluate the mean values of $X = r^2$ or $X = \phi$.

However, to compute their standard deviations

$$\sigma(X) = \sqrt{\langle X^2\rangle - \langle X\rangle^2}\,, \tag{C.1.4}$$

we need to evaluate $\langle X^2\rangle$, where we have to include terms up to 4-th order in the disorder parameters $\tilde{x}_k$. Here we can make use of Wick's theorem [18], from which one can conclude that higher-order expectation values of Gaussian variables can be decomposed into the sum of all possible products of second-order expectation

values, *e.g.*,

$$\begin{aligned}\langle x_m x_n x_r x_s\rangle &= \langle x_m x_n\rangle\langle x_r x_s\rangle + \langle x_m x_r\rangle\langle x_n x_s\rangle + \langle x_m x_s\rangle\langle x_n x_r\rangle \\ &= \delta_{mn}\delta_{rs} + \delta_{mr}\delta_{ns} + \delta_{ms}\delta_{nr}\,. \end{aligned} \tag{C.1.5}$$

From the fact that $\langle x_m\rangle = 0$, we can directly conclude that all expectation values of odd order are automatically zero. For the Fourier components we obtain with Eq. (4.2.20) correspondingly

$$\begin{aligned}\langle \tilde{x}_k\tilde{x}_l\tilde{x}_p\tilde{x}_q\rangle &= \frac{1}{N^2}\sum_{mnrs}\langle x_m x_n x_r x_s\rangle e^{2\pi ik(m-1)/N} e^{2\pi il(n-1)/N} e^{2\pi ip(r-1)/N} e^{2\pi iq(s-1)/N} \\ &= \delta_{k,-l}\;\delta_{p,-q} + \delta_{k,-p}\;\delta_{l,-q} + \delta_{k,-q}\;\delta_{l,-p}\,, \end{aligned} \tag{C.1.6}$$

and similarly for the Dirac approach.

C.2. Scattering matrix for preserved chiral symmetry for small boundary lengths

As stated in Section 4.2.4, for preserved chiral symmetry we cannot derive exact expressions for the parameters r^2 and ϕ of the scattering matrix depending on the boundary length $L = Na$. To still have analytical expressions as a reference, we can however compute expressions for the lowest possible lengths $N = 3$ and $N = 6$.

From Eqs. (4.2.14), (4.2.15) we obtain with Eq. (4.2.19) for $N = 3$

$$r_3^2 = \frac{4}{3}V^2|\tilde{x}_1|^2 + \mathcal{O}(V^3)\,, \tag{C.2.1}$$

$$\phi_3 = -\sqrt{\frac{4}{3}}V\tilde{x}_0 + \mathcal{O}(V^3)\,. \tag{C.2.2}$$

From these expressions using the considerations of Appendix C.1 we directly obtain Eq. (4.2.32).

For $N = 6$ we obtain analogously

$$r_6^2 = \frac{2V^2F(\tilde{x}_0,\tilde{x}_1,\tilde{x}_2)}{3\tilde{x}_0^2 + V^2\Big((\tilde{x}_0^2 - |\tilde{x}_1|^2)^2 + F(\tilde{x}_0,\tilde{x}_1,\tilde{x}_2)\Big)}\,, \tag{C.2.3}$$

with

$$F(\tilde{x}_0,\tilde{x}_1,\tilde{x}_2) = |\tilde{x}_1|^4 - \tilde{x}_0\Big((\tilde{x}_1^*)^2\tilde{x}_2 + \tilde{x}_1^2\tilde{x}_2^*\Big) + |\tilde{x}_0|^2|\tilde{x}_2|^2\,. \tag{C.2.4}$$

For $V \ll 1$, r_6^2 as a function of $\tilde{x}_0$ is very sharply centered around $\tilde{x}_0 = 0$. Thus, we can replace $\tilde{x}_0$ by 0 in the terms $\propto V^2$, such that we remain with

$$r_6^2 \approx \frac{2V^2|\tilde{x}_1|^4}{3\tilde{x}_0^2 + 2V^2|\tilde{x}_1|^4}\,. \tag{C.2.5}$$

Furthermore, with the same reasoning we can approximate the probability distribution of $\tilde{x}_0$ as

$$\tilde{f}(\tilde{x}_0) = \frac{1}{\sqrt{2\pi}} e^{-\tilde{x}_0^2/2} \approx \frac{1}{\sqrt{2\pi}}\,. \tag{C.2.6}$$

With this, we can evaluate

$$\langle r_6^2 \rangle \approx \frac{1}{\sqrt{2\pi}} \int \mathrm{d}\tilde{x}_0 \int \mathrm{d}\tilde{x}_1 \tilde{f}(\tilde{x}_1)\; r_6^2 = \sqrt{\frac{\pi}{3}}\; V \int \mathrm{d}\tilde{x}_1 \tilde{f}(\tilde{x}_1)|\tilde{x}_1|^2 = \sqrt{\frac{\pi}{3}}\; V\,, \tag{C.2.7}$$

$$\langle r_6^4 \rangle \approx \frac{1}{\sqrt{2\pi}} \int \mathrm{d}\tilde{x}_0 \int \mathrm{d}\tilde{x}_1 \tilde{f}(\tilde{x}_1)\; r_6^4 = \frac{1}{2}\sqrt{\frac{\pi}{3}}\; V \int \mathrm{d}\tilde{x}_1 \tilde{f}(\tilde{x}_1)|\tilde{x}_1|^2 = \frac{1}{2}\sqrt{\frac{\pi}{3}}\; V\,, \tag{C.2.8}$$

and

$$\sigma(r_6^2) = \sqrt{\langle r_6^4 \rangle - \langle r_6^2 \rangle^2} = \sqrt[4]{\frac{\pi}{12}}\sqrt{V} + \mathcal{O}(V^{3/2})\,. \tag{C.2.9}$$

For the scattering phase ϕ we obtain

$$\phi_6 = \arctan\left(\sqrt{\frac{2}{3}}\; \frac{|\tilde{x}_1|^2 - \tilde{x}_0^2}{\tilde{x}_0}\; V + \mathcal{O}(V^3)\right)\,. \tag{C.2.10}$$

This is an odd function of $\tilde{x}_0$, hence we directly see that averaging over $\tilde{x}_0$ yields $\langle \phi_6 \rangle = 0$. For the standard deviation of ϕ_6 we have to compute

$$\begin{aligned}\langle \phi_6^2 \rangle &= \left\langle \arctan^2\left(\sqrt{\frac{2}{3}}\; \frac{|\tilde{x}_1|^2 - \tilde{x}_0^2}{\tilde{x}_0}\; V\right)\right\rangle + \mathcal{O}(V^6) \\ &= \left\langle \arctan^2\left(\sqrt{\frac{2}{3}}\; \frac{|\tilde{x}_1|^2}{\tilde{x}_0}\; V\right)\right\rangle + \mathcal{O}(V^2)\,,\end{aligned} \tag{C.2.11}$$

where the last approximation comes from the fact that $\tilde{x}_0$ is Gaussian distributed around zero and therefore under the integral over $\tilde{x}_0$ the term $\propto 1/\tilde{x}_0$ in the arctangent dominates over the term $\propto \tilde{x}_0$. As $\arctan^2(\epsilon/\tilde{x}_0)$ is a very sharp function

of $\tilde{x}_0$ around zero for small ϵ, we can again use the approximation Eq. (C.2.6) and compute

$$\int_{-\infty}^{\infty} \frac{\mathrm{d}\tilde{x}_0}{\sqrt{2\pi}} \arctan^2\left(\frac{\epsilon}{\tilde{x}_0}\right) = \int_{-\infty}^{\infty} \frac{\mathrm{d}\tilde{x}_0}{\sqrt{2\pi}} \int_0^{\epsilon} \frac{\mathrm{d}\epsilon_1}{\tilde{x}_0(1+\epsilon_1^2/\tilde{x}_0^2)} \int_0^{\epsilon} \frac{\mathrm{d}\epsilon_2}{\tilde{x}_0(1+\epsilon_2^2/\tilde{x}_0^2)}$$

$$\underset{\substack{\text{complex}\\ \text{contour}\\ \text{integration}}}{=} \sqrt{\frac{\pi}{2}} \int_0^{\epsilon} \int_0^{\epsilon} \frac{\mathrm{d}\epsilon_1\, \mathrm{d}\epsilon_2}{|\epsilon_1| + |\epsilon_2|} = \sqrt{2\pi}\ln(2)\,|\epsilon|\,. \tag{C.2.12}$$

With $\epsilon = \sqrt{2/3}\; V|\tilde{x}_1|^2$ we eventually obtain

$$\sigma(\phi_6) = \sqrt{\langle \phi_6^2 \rangle} = \sqrt{\sqrt{\frac{4\pi}{3}}\ln(2)}\;\sqrt{V} + \mathcal{O}(V)\,. \tag{C.2.13}$$

Acknowledgements

First and foremost, I would like to thank Prof. Dr. Fabian Hassler for giving me the opportunity to work with him during the last year. He did an excellent job in supervising me and always had time for discussions, not only about all kinds of physical issues, but also about problems in society, technology, politics, and how difficult it is to fly a helicopter in the Alps. All in all, the work on this project was very diverse and very instructive.

My special thanks go to Prof. Dr. Anton Akhmerov from TU Delft, who has made substantial contributions to the success of this work. In a lot of fruitful discussions he shared his creative ideas with us that often helped the progress of this project.

I wish to thank Prof. Dr. Christoph Stampfer, who kindly agreed to be my second supervisor.

Many thanks go

to Florian Venn, who seems to have profound knowledge not only about all areas of physics, but also about IT infrastructure, and was therefore the perfect office mate for stupid questions of all kind that occur from time to time, and help with setting up computations on the cluster,

and to all the staff in the IQI for countless discussions, lunch breaks, excellent cakes, after work beer, and the friendly and nice atmosphere.

Eventually, I want to thank Lisa Tischer for proofreading this thesis and for constant support in all manners, and my family for all support in the last year and the last decades.

Bibliography

[1] Castro Neto, A. H., Guinea, F., Peres, N. M. R., Novoselov, K. S., and Geim, A. K. *The electronic properties of graphene.* Rev. Mod. Phys., **81** (109), 2009.

[2] Wallace, P. R. *The band theory of graphite.* Phys. Rev., **71** (622), 1947.

[3] Semenoff, G. W. *Condensed-matter simulation of a three-dimensional anomaly.* Phys. Rev. Lett., **53** (2449), 1984.

[4] Geim, A. K. and Novoselov, K. S. *The rise of graphene.* Nature Mater., **6** (183), 2007.

[5] Novoselov, K. S., Geim, A. K., Morozov, S. V., Jiang, D., Zhang, Y., Dubonos, S. V., Grigorieva, I. V., and Firsov, A. A. *Electric field effect in atomically thin carbon films.* Science, **306** (666), 2004.

[6] Novoselov, K. S., Geim, A. K., Morozov, S. V., Jiang, D., Katsnelson, M. I., Grigorieva, I. V., Dubonos, S. V., and Firsov, A. A. *Two-dimensional gas of massless Dirac fermions in graphene.* Nature, **438** (197), 2005.

[7] Kungl. Vetenskaps-Akademien. *Scientific Background on the Nobel Prize in Physics 2010: Graphene*, 2010.

[8] Cheng, R., Bai, J., Liao, L., Zhou, H., Chen, Y., Liu, L., Lin, Y.-C., Jiang, S., Huang, Y., and Duan, X. *High-frequency self-aligned graphene transistors with transferred gate stacks.* Proc. Natl. Acad. Sci. USA, **109** (11588), 2012.

[9] Banszerus, L., Schmitz, M., Engels, S., Goldsche, M., Watanabe, K., Taniguchi, T., Beschoten, B., and Stampfer, C. *Ballistic transport exceeding* $28\,\mu m$ *in CVD grown graphene.* Nano Letters, **16** (1387), 2016.

[10] Akhmerov, A. R. and Beenakker, C. W. J. *Boundary conditions for Dirac fermions on a terminated honeycomb lattice.* Phys. Rev. B, **77** (085423), 2008.

[11] McCann, E. and Fal'ko, V. I. *Symmetry of boundary conditions of the Dirac equation for electrons in carbon nanotubes.* J. Phys. Condens. Matter, **16** (2371), 2004.

[12] Son, Y.-W., Cohen, M. L., and Louie, S. G. *Energy gaps in graphene nanoribbons.* Phys. Rev. Lett., **97** (216803), 2006.

[13] Berry, M. V. and Mondragon, R. J. *Neutrino billiards: time-reversal symmetry-breaking without magnetic fields.* Proc. R. Soc. Lond. A, **412** (53), 1987.

[14] Groth, C. W., Wimmer, M., Akhmerov, A. R., and Waintal, X. *Kwant: a software package for quantum transport.* New J. Phys., **16** (063065), 2014.

[15] Dresen, D. *Quantum transport of non-interacting electrons in 2D systems of arbitrary geometries.* Master's thesis, RWTH Aachen University, 2014.

[16] Sherman, J. and Morrison, W. J. *Adjustment of an inverse matrix corresponding to a change in one element of a given matrix.* Ann. Math. Statist., **21** (124), 1950.

[17] Trench, W. F. *Explicit inversion formulas for Toeplitz band matrices.* SIAM J. Alg. Disc. Meth., **6** (546), 1985.

[18] Wick, G. C. *The evaluation of the collision matrix.* Phys. Rev., **80** (268), 1950.